

Article

Numerical Study of Velocity and Mixture Fraction Fields in a Turbulent Non-Reacting Propane Jet Flow Issuing into Parallel Co-Flowing Air in Isothermal Condition through OpenFOAM

Abdolreza Aghajanpour ^{1,*} and Seyedalireza Khatibi ²

¹ Barcelona School of Civil Engineering, Universitat Politècnica de Catalunya (UPC-BarcelonaTech), 08034 Barcelona, Spain

² Petroleum Engineering Department, University of North Dakota, Grand Forks, ND 58202, USA; ali68khatibi@gmail.com

* Correspondence: abdolreza.aghajanpour@estudiantat.upc.edu

Abstract: This research employs computational methods to analyze the velocity and mixture fraction distributions of a non-reacting Propane jet flow that is discharged into parallel co-flowing air under isothermal conditions. This study includes a comparison between the numerical results and experimental results obtained from the Sandia Laboratory (USA). The objective is to improve the understanding of flow structure and mixing mechanisms in situations where there is no involvement of chemical reactions or heat transfer. In this experiment, the Realizable $k-\epsilon$ eddy viscosity turbulence model with two equations was utilized to simulate turbulent flow on a nearly 2D plane (specifically, a 5-degree partition of the experimental cylinder domain). This was achieved using OpenFOAM open-source software and swak4Foam utility, with the reactingFoam solver being manipulated carefully. The selection of this turbulence model was based on its superior predictive capability for the spreading rate of both planar and round jets, as compared to other variants of the $k-\epsilon$ models. Numerical axial and radial profiles of different parameters were obtained for a mesh that is independent of the grid (mesh B). These profiles were then compared with experimental data to assess the accuracy of the numerical model. The parameters that are being referred to are mean velocities, turbulence kinetic energy, mean mixture fraction, mixture fraction half radius (L_f), and the mass flux diagram. The validity of the assumption that $w' = v'$ for the determination of turbulence kinetic energy, k , seems to hold true in situations where experimental data is deficient in w' . The simulations have successfully obtained the mean mixture fraction and its half radius, L_f , which is a measure of the jet's width. These values were determined from radial profiles taken at specific locations along the X-axis, including $x/D = 0, 4, 15, 30,$ and 50 . The accuracy of the mean vertical velocity fields in the X-direction (U_{mean}) is noticeable, despite being less well-captured. The resolution of mean vertical velocity fields in the Y-direction (V_{mean}) is comparatively lower. The accuracy of turbulence kinetic energy (k) is moderate when it is within the range of U_{mean} and V_{mean} . The absence of empirical data for absolute pressure (p) is compensated by the provision of numerical pressure contours.

Keywords: turbulence modeling; non-reaction Propane jet; Realizable $k-\epsilon$ eddy viscosity turbulence model; OpenFOAM; swak4Foam



Citation: Aghajanpour, A.; Khatibi, S. Numerical Study of Velocity and Mixture Fraction Fields in a Turbulent Non-Reacting Propane Jet Flow Issuing into Parallel Co-Flowing Air in Isothermal Condition through OpenFOAM. *AppliedMath* **2023**, *3*, 468–496. <https://doi.org/10.3390/appliedmath3020025>

Academic Editor: Carlo Bianca

Received: 10 April 2023

Revised: 9 May 2023

Accepted: 12 May 2023

Published: 27 May 2023



Copyright: © 2023 by the authors. Licensee MDPI, Basel, Switzerland. This article is an open access article distributed under the terms and conditions of the Creative Commons Attribution (CC BY) license (<https://creativecommons.org/licenses/by/4.0/>).

1. Introduction

Axisymmetric nozzle jets are a significant type of free shear layer flows that exhibit turbulence. The primary phenomenon is turbulence caused by the velocity gradient and instabilities between the jet and the surrounding fluid [1]. Reactive flows are recognized as beneficial constituents of turbulent jets and are extensively employed in diverse sectors, including combustion and military engineering. The complexity of addressing these jets stems from the interaction between turbulent mixing and heat release caused by chemical reactions [2,3].

The process of modeling turbulent reacting flows relies numerically on models that were originally developed for constant-density flows that do not involve any chemical reactions. The efficacy of utilizing said models may be inadequate in terms of authenticity. The utilization of a turbulent, non-reacting variable-density jet can streamline the issue at hand while retaining the intricacy of variable density. This approach also eliminates the requirement to account for the interplay between turbulent mixing and chemical heat release, as stated in reference [3]. Numerous experimental investigations have been carried out on turbulent jets with constant density, as documented in references [4–8]. Several experiments have been conducted on strongly variable-density jets using axisymmetric nozzles, as documented in references [9–17]. Advanced laser technology has facilitated a comprehensive analysis of the reactive behavior of turbulent jets, as reported in references [18,19].

The inlet conditions, including injection ratio, co-flow direction, and nozzle geometry, have an impact on the features of variable-density turbulent jets [2,20]. The injection ratio is a key parameter that has a significant impact on the initial mixing and subsequent development of a jet [20]. It is defined as the ratio of the momentum flux of the jet to that of the ambient fluid. According to reference [2], the flow structure, turbulence levels, and mixing processes within a jet can be modified by the direction and magnitude of the co-flowing fluid, thereby influencing the behavior of the jet. The behavior of a jet is significantly impacted by the geometry of its nozzle, which affects both its initial velocity and turbulence intensity. The development of a jet, specifically its entrainment and spread, can be influenced by the shape of the nozzle, as documented in reference [2]. The precise modeling and forecasting of turbulent jets with variable densities necessitate meticulous attention to inlet conditions. Understanding the influence of these factors on the dynamics of jet flow and turbulent mixing is essential for a range of industrial applications, such as combustion, mixing, and heat transfer processes. The study of the effects of inlet conditions on variable-density turbulent jets is a prominent area of research that can provide valuable insights into the complex behavior of these flows.

Gonçalves et al. performed numerical simulations of a turbulent non-premixed, and non-reacting Propane jet flow in the presence of co-flowing air using the Unsteady Reynolds Averaged Navier-Stokes (URANS) modeling and Standard $k-\epsilon$ model. Furthermore, they used an adaptive refinement in the mesh domain to reduce the computational cost. They finally compared numerical results for velocity and mixture fraction at the jet center line with experimental data for validation and observed a satisfactory performance of their approach [21].

The spatial development of air-air compressible coaxial jets was numerically simulated by Ouzani R et al. using 3D-Monotone Integrated Large Eddy Simulations (MILES). The computations were performed on isothermal and non-isothermal coaxial jets. The spatiotemporal evolution of the mixture fraction field is utilized to track the mixing between inner and outer jets. The spatially developing approach is a method that considers the various phases of turbulent mixing, including molecular diffusion, transition, and fully developed turbulent state. The results obtained were found to be satisfactory and in good agreement with the experimental data. The examination of mixture fraction fluctuations suggests that the onset of turbulent mixing occurs earlier in the non-isothermal scenario. The statement is consistent with the early formation of the Kelvin–Helmholtz vortices [22].

The objective of this study is to assess the efficacy of the Realizable $k-\epsilon$ eddy viscosity turbulence model in reproducing the outcomes of experiments conducted on a turbulent axisymmetric jet. The objective was achieved by utilizing and modifying one of the standard solvers in OpenFOAM 5 (i.e., ReactingFoam) with the assistance of SWiss Army Knife for Foam (Swak4Foam). The reactingFoam is intended to tackle mixing issues in compressible flows that involve combustion and reactions. The performance of the model can be assessed and confirmed by simulating the experimental data obtained from the TNF data archive, which can be accessed at <http://www.sandia.gov/TNF/DataArch/ProJet.html> (accessed on 10 March 2023).

The Realizable k - ϵ turbulence model is a well-established and widely employed model in the field of fluid dynamics for the purpose of forecasting turbulent flows. This model has been validated and is frequently utilized for the prediction of turbulent jets that do not involve any chemical reactions [1]. The employed model is a modified variant of the Standard k - ϵ model. It accounts for the influence of turbulence anisotropy and compressibility. The methodology utilized is founded upon the Reynolds-Averaged Navier-Stokes (RANS) equations. The model effectively resolves intricate turbulence structures and mixing processes occurring within the jet, thereby offering significant insights into flow dynamics and turbulent mixing phenomena. The Realizable k - ϵ eddy viscosity turbulence model, in conjunction with numerical simulations, provides a cost-effective and efficient method for investigating turbulent axisymmetric jets. The aforementioned approach offers significant advantages over experimental research as it enables accurate control of inlet conditions and overcomes practical constraints inherent in physical experiments. The results of this study can assist in improving the accuracy and reliability of computational tools used for predicting turbulent jet dynamics. The aforementioned can result in noteworthy consequences for diverse industrial implementations.

In the present numerical study, the Realizable k - ϵ eddy viscosity turbulence model with two equations was utilized for the first time in this specific test case. The model was used to simulate turbulent flow on an approximate 2D plane (specifically a 5-degree partition of the cylinder of the experimental domain). The simulation was conducted using OpenFOAM 5 and the swak4Foam utility, with the reactingFoam solver being meticulously manipulated. The initial step for modeling a turbulent axisymmetric jet in this research involved selecting the sandiaD_LTS tutorial (located in combustion > reactingFoam > RAS) to begin the process of manipulating the numerical test cases. The tutorial case concerns a reacting flow, but the study has excluded combustion and chemical reaction from the experiment as they are not observed. The reactingFoam solver's robust features were utilized to achieve a precise simulation of a non-reacting jet through this methodology. The accuracy and reliability of the selected modeling approach can be assessed by comparing the simulation outcomes with the experimental data.

2. Numerical Basement

2.1. Mixture Fraction Theory

Non-premixed combustion is a type of combustion where the fuel and oxidizer are introduced into the reaction zone separately. This is in contrast with the premixed systems, where the fuel and oxidizer are already mixed before entering the reaction zone. This observation has been documented in prior research [23]. Under certain conditions, it is possible to simplify thermochemistry to a solitary parameter known as the mixture fraction (f). The parameter in question denotes the proportion of mass obtained from the fuel stream and is a scalar quantity that remains constant. The transport equation governing it does not contain a source term. Combustion can be reduced to a mixing problem. Chemical modeling can be performed using various methods, such as the Equilibrium model, Steady Diffusion Flamelet, or Unsteady Diffusion Flamelet. The selection of the appropriate method depends on the degree of proximity to chemical equilibrium. The details regarding this can be found in reference [23].

The assumption of equal diffusivities of species can pose difficulties for laminar flows. However, it is typically deemed acceptable for turbulent flows, as turbulent convection tends to be more dominant than molecular diffusion. The equations pertaining to the species can be reduced to a single transport equation that governs the mixture fraction, denoted as f . The process of non-premixed modeling involves the solution of the following equation. The mixture fraction field that is predicted can be utilized to ascertain the species concentration. Under specific simplifying assumptions, the mixture fraction can be correlated to the thermochemical state of the fluid. The approach of modeling mixture fractions reduces the complexity of chemistry to one or two conserved mixture fractions, thereby providing a significant advantage. According to chemical equilibrium, thermochemical properties,

such as species fractions, density, and temperature, have a distinct correlation with mixture fraction(s) [23].

2.2. The Transport Equation for the Mixture Fraction

The Favre mean (density-averaged) mixture fraction equation is [23]

$$\frac{\partial(\rho\bar{f})}{\partial t} + \nabla \cdot (\rho\vec{v}\bar{f}) = \nabla \cdot (\rho\vec{v}\bar{f}) + \frac{\partial}{\partial x_j} \left(\frac{\mu_l + \mu_t}{\sigma_f} \nabla \bar{f} \right)$$

3. Description of Computational Domain and Assumptions

The axisymmetric assumption is deemed reasonable based on a comparison between the inner and outer dimensions of the tube and the horizontal cross-section of the experimental domain. Additionally, the significant difference in bulk velocity between Propane and co-flowing air supports this assumption. This hypothesis has the potential to decrease the computational resources needed substantially. The computational domain is constrained to a nearly 2D plane, which is precisely a sector of the 5-degree of the largest cylinder that can be embedded in the real domain.

There are two distinct approaches to the preparation of computational geometry. In the first one, the sector can be defined by disregarding the length of the nozzle. Consequently, the simulation will not include the flow inside the nozzle. In this scenario, the inlets for Propane and co-flowing air will be located at the level of the nozzle exhaust.

In the other approach (as in this study), an alternative method was employed, similar to the other approach, where a 10 cm nozzle was placed upstream to aid in achieving fully developed flow within the nozzle. Pre-injection was performed to improve the development of the boundary layer between the co-flowing air and the outer edge of the nozzle, as observed during experimentation. This was performed before injecting the mixture into the main computational domain. The primary approach is characterized by reduced cell quantities, resulting in cost-effectiveness and efficiency. However, it may exhibit lower precision levels as it may not entirely replicate the actual boundary conditions that surround the nozzle's structure.

The Realizable $k-\epsilon$ model utilizes a variable function for the coefficient C_μ in the equation for turbulent viscosity (ν_t), which distinguishes it from the Standard $k-\epsilon$ model where C_μ is a constant. The transport equation governing Turbulence Kinetic Energy (k) is the same in both the Standard and Realizable $k-\epsilon$ models, except for variations in model constants. The transport equation for Dissipation Rate (ϵ) has been modified by segregating it from the precise equation for the transportation of mean-square vorticity fluctuations. The aforementioned modification is significant. The Realizable $k-\epsilon$ model outperforms all other versions of the $k-\epsilon$ models in accurately predicting the spreading rate of planar and round jets [24].

The computational domain in this study has been restricted to a distance of 100 cm ($x/D = 190$), as determined by the graphical representation of the experimental data. No significant variations were detected beyond the value of x/D greater than 80. The co-flowing air is composed of N_2 and O_2 with volume fractions of 0.7632 and 0.2368, respectively. It is assumed that the flow is compressible and isothermal at a temperature of 294 K. The injected fluid is considered to be an ideal gas.

The system folder contains the blockMeshDict, changeDictionaryDict, and extrudeMeshDict files. The simulation domain's boundaries were established and modified through the utilization of the blockMeshDict file and its corresponding files for each variable located in the 0 folders. The boundaries of the system are defined as follows: inletfuel, which represents the inlet boundary of Propane upstream on the inner diameter of the nozzle; inletair, which represents the inlet boundary of co-flowing air at the upstream, from the outer ridge of the nozzle to the lateral border on the left side; outlet, which represents the downstream outlet boundary; axis, which represents the symmetry axis for sector rotation; leftside, which represents the

lateral edge of the domain; burnerwall, which represents the part of upstream boundaries that represents the nozzle body; and front and back, which are used for simulating a 2D problem.

A simplified scheme of the computational domain is depicted in Figure 1. It should be noted, X, Y and Z are the selected axes in the modeling and solution process throughout the paper.

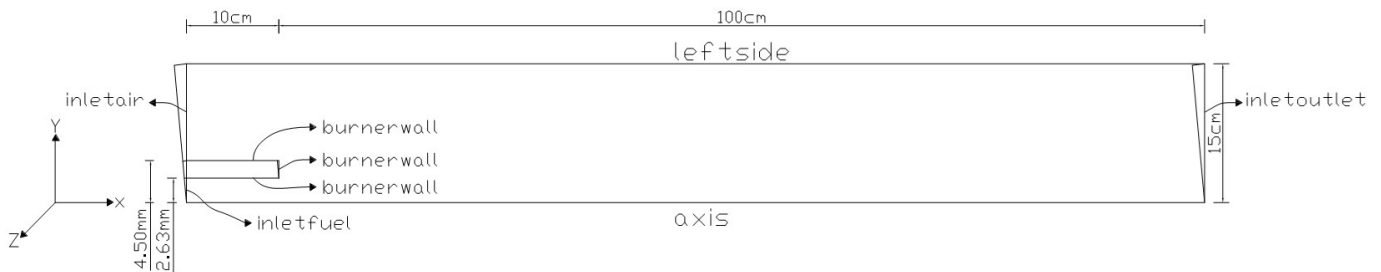


Figure 1. The simplified scheme of the computational domain.

The grids were adjusted in the X and Y directions of each block in the blockMeshDict file using a predefined lengthGrading. This was performed to reduce computational costs and achieve a suitable aspect ratio.

The calculation of turbulence kinetic energy, denoted as k , can be achieved through the following formulations:

$$U_{RMS} = \sqrt{\overline{u'^2}}, V_{RMS} = \sqrt{\overline{v'^2}}, W_{RMS} = \sqrt{\overline{w'^2}}$$

$$\Rightarrow U_{RMS}^2 = \overline{u'^2}, V_{RMS}^2 = \overline{v'^2}, W_{RMS}^2 = \overline{w'^2}$$

$$k = \frac{1}{2}(\overline{u'^2} + \overline{v'^2} + \overline{w'^2}) = \frac{1}{2}(U_{RMS}^2 + V_{RMS}^2 + W_{RMS}^2)$$

However, based on the experimental data, it is suggested that a 2D assumption can be made, resulting in a simplification of the model to

$$k = \frac{1}{2}(U_{RMS}^2 + V_{RMS}^2 + W_{RMS}^2) = \frac{1}{2}(U_{RMS}^2 + 2V_{RMS}^2)$$

Non-dimensional parameters were plotted at the outset. An assessment was performed on the axial and radial profiles of various parameters, including average velocities, turbulence energy, average mixture fraction, and a half radius of the mixture fraction. Subsequently, the pressure (p) was demonstrated in the results. A figure is presented to compare the obtained Total Kinetic Energy, k , results for all four test cases. The comparison is made at the center line and at x/D values of 15, 30, and 50. A comparison was made between the numerical and experimental data for every parameter.

Table 1 provides a concise presentation of the computational domain's dimensions and inlet data:

Table 1. Concise list of computational domain's dimensions and inlet data.

Orientation	Vertical
Inner Diameter of the Nozzle ($D/2$)	(0.526)/2 cm
Outer Diameter of the Nozzle	(0.90)/2 cm
The Length of the Domain	100 cm
The Width of the Domain	30/2 cm
Propane Jet's Bulk Velocity	53 m/s
Propane Jet's Temperature	294 K
Co-flowing Air's Velocity	9.2 m/s

Table 1. Cont.

Orientation	Vertical
Co-flowing Air's Temperature	294 K
Reynolds number (based on D)	68,000 (68,168 in velstat files)
Co-flowing Air's Turbulence Intensity	0.4%

4. Initial and Boundary Conditions of Variables

The meshes provided indicate that the final computational node located on the leftside will be positioned beyond the boundary layer. It is crucial for the accuracy of the wall functions assumption that Y-plus is not restricted to a range of 30 to 100. Therefore, the utilization of wall functions is prohibited. However, for reasons of numerical cost, it is not advisable to increase the mesh resolution towards the outer walls, specifically the leftside.

The initial method involves adopting a boundary condition of fixedValue, with a value of 9.2 assigned to the velocity variable U, while the other variables are subjected to a zeroGradient boundary condition. The leftside boundary is subjected to a simulated slip condition in an attempt to closely approximate reality. It is expected that the meshes have undergone adequate refinement on both the inner and outer surfaces of the nozzle body, particularly on the burnerwall. The variables alphas, epsilon, k, and nut were subjected to a wall function, whereas U was subjected to a no-slip condition.

Furthermore, a secondary method was utilized to authenticate the accuracy of the assumptions made regarding the burnerwall of the nozzle. The process required the partitioning of the boundary into three distinct sides, namely, burnerwall_jet, burnerwall_air, and burnerwall_upper. Subsequently, specific boundary conditions were allocated to each side with respect to the variables. This study did not provide numerical results. However, the absence of significant differences indicates that the first approach's assumptions are valid.

The first approach's initial and boundary conditions for different variables are presented in Tables 2 and 3.

Table 2. Compilation of initial and boundary conditions for variables in the first approach.

Variable	Inletfuel	Inletair	Outlet	Dimensions
alpha	calculated	calculated	calculated	[1 -1 -1 0 0 0]
C ₃ H ₈	fixedValue (=1.0)	fixedValue (=0.0)	inletOutlet	[0 0 0 0 0 0]
epsilon	turbulentMixingLengthDissipationRateInlet	turbulentMixingLengthDissipationRateInlet	inletOutlet	[0 2 -3 0 0 0]
k	turbulentIntensityKineticEnergyInlet	turbulentIntensityKineticEnergyInlet	inletOutlet	[0 2 -2 0 0 0]
N ₂	fixedValue (=0.0)	fixedValue (=0.763149)	inletOutlet	[0 0 0 0 0 0]
nut	calculated	calculated	calculated	[0 2 -1 0 0 0]
O ₂	fixedValue (=0.0)	fixedValue (=0.236851)	inletOutlet	[0 0 0 0 0 0]
p	zeroGradient	zeroGradient	totalPressure	[1 -1 -2 0 0 0]
T	fixedValue (=294)	fixedValue (=294)	inletOutlet	[0 0 0 1 0 0]
U	fixedValue (=53)	fixedValue (=9.2)	pressureInletOutletVelocity	[0 1 -1 0 0 0]

The variables have been initialized as empty at the boundary of the axis. This boundary is considered an edge rather than a surface of the domain. The wedge has been assigned to serve as the front and back boundaries owing to their repetitive nature as two sides of the sector.

Table 3. List of initial and boundary conditions for various variables in the first approach.

Variable	Leftside	Burnerwall	Internal Field	Dimensions
alphan	zeroGradient	Compressible:alphan WallFunction	0	[1 -1 -1 0 0 0]
C ₃ H ₈	zeroGradient	zeroGradient	0	[0 0 0 0 0 0]
epsilon	zeroGradient	epsilonWallFunction	200	[0 2 -3 0 0 0]
k	zeroGradient	kqWallFunction	1	[0 2 -2 0 0 0]
N ₂	zeroGradient	zeroGradient	0.7632	[0 0 0 0 0 0]
nut	zeroGradient	nutkWallFunction	0	[0 2 -1 0 0 0]
O ₂	ZeroGradient	zeroGradient	0.2368	[0 0 0 0 0 0]
p	zeroGradient	zeroGradient	101,325	[1 -1 -2 0 0 0]
T	zeroGradient	zeroGradient	294	[0 0 0 1 0 0]
U	fixedValue (=9.2)	fixedValue (=0.0)	9.2	[0 1 -1 0 0 0]

The present study involves the analysis of the injection of a fully turbulent Propane jet into the domain. Thus, the Turbulent Intensity (I), which represents the turbulence level at the interior boundary, and the boundary conditions for Turbulence Kinetic Energy (k) and its Dissipation Rate (ε) are successively calculated using a constant value of C_μ = 0.09, as reported in reference [23]:

$$\begin{aligned}
 I_{inlet,fuel} &= 0.16Re_{D,fuel}^{-\frac{1}{8}} \simeq 0.0398 \\
 k_{inlet,fuel} &= \frac{3}{2}(U.I)^2 \simeq 6.679 \\
 l_{inlet,fuel} &= 0.07D_{h,fuel} = 0.000368m \\
 \epsilon_{inlet} &= C_{\mu}^{\frac{3}{4}}k_{inlet,fuel}^{\frac{3}{2}}l_{inlet,fuel}^{-1} \simeq 5630
 \end{aligned}$$

Similarly, in the context of injecting the turbulent air into the domain from the inletair boundary, the following procedure can be applied:

$$\begin{aligned}
 k_{inlet,air} &= \frac{3}{2}(U.I)^2 \simeq 0.002 \\
 l_{inlet,air} &= 0.07D_{h,air} = 0.021m \\
 \epsilon_{inlet,air} &= C_{\mu}^{\frac{3}{4}}k_{inlet,air}^{\frac{3}{2}}l_{inlet,air}^{-1} \simeq 0.0006998
 \end{aligned}$$

While it is understood that the boundary conditions, rather than the initial values, determine the steady-state results, it is still common practice to assign appropriate initial values to the variables for logical consistency.

5. Other Governing Equations

5.1. Mass Conservation Equation [23]

Mass conservation equation is as follows:

$$\frac{\partial \rho}{\partial t} + \nabla \cdot (\rho \vec{U}) = 0$$

5.2. Energy Conservation Equation [23]

Energy conservation equation is as follows:

$$\frac{\partial}{\partial t}(\rho E) + \nabla \cdot (\vec{U}(\rho E + p)) = -\nabla \sum_j h_j J_j + S_h$$

5.3. Momentum Conservation Equation [23]

Momentum conservation equation is as follows:

$$\frac{\partial(\rho\vec{U})}{\partial t} + \nabla \cdot (\rho\vec{U}\vec{U}) = -\nabla p + \rho\vec{g} + \vec{F}$$

5.4. Transport Equations for Turbulence Kinetic Energy, k, and Its Dissipation Rate, ε, [24,25]

Transport equations for turbulence kinetic energy are as follows:

$$\begin{aligned} \frac{\partial(\rho k)}{\partial t} + \frac{\partial(\rho k u_j)}{\partial x_j} &= \frac{\partial}{\partial x_j} \left[\left(\mu + \frac{\mu_t}{\sigma_k} \right) \frac{\partial k}{\partial x_j} \right] + G_k + G_b - \rho \varepsilon - Y_M + S_k \\ \frac{\partial(\rho \varepsilon)}{\partial t} + \frac{\partial(\rho \varepsilon u_j)}{\partial x_j} &= \frac{\partial}{\partial x_j} \left[\left(\mu + \frac{\mu_t}{\sigma_\varepsilon} \right) \frac{\partial \varepsilon}{\partial x_j} \right] + C_1 \rho |S| \varepsilon - C_2 \rho \frac{\varepsilon^2}{k + \sqrt{\nu \varepsilon}} + C_{1\varepsilon} \frac{\varepsilon}{k} C_{3\varepsilon} G_b + S_\varepsilon \\ G_k &= -\rho \overline{u'_i u'_j} = \mu_t S^2; C_1 = \max \left[0.43, \frac{\eta}{\eta + 5} \right]; \eta = S \frac{k}{\varepsilon}; S \equiv \sqrt{2 S_{ij} S_{ij}} \\ C_2 &= 1.9; \sigma_k = 1; \sigma_\varepsilon = 1.2; \\ \nu_t &= C_\mu \frac{k^2}{\varepsilon}; C_\mu = \frac{1}{A_0 + A_s U^* \frac{k}{\varepsilon}}; A_0 = 4.04 \\ A_s &= \sqrt{6} \cos \phi; \phi = \frac{1}{6} \cos^{-1} (W \sqrt{6}); W = \frac{S_{ij} S_{jk} S_{ki}}{\tilde{S}^3}; \tilde{S} = \sqrt{S_{ij} S_{ij}}; S_{ij} = \frac{1}{2} \left(\frac{\partial u_j}{\partial x_i} + \frac{\partial u_i}{\partial x_j} \right) \\ U^* &= \sqrt{S_{ij} S_{ij} + \tilde{\Omega}_{ij} \tilde{\Omega}_{ij}}; \tilde{\Omega}_{ij} = \Omega_{ij} - 2 \varepsilon_{ijk} \omega_k; \Omega_{ij} = \tilde{\Omega}_{ij} - \varepsilon_{ijk} \omega_k \end{aligned}$$

6. Numerical Discretizing Schemes

Table 4 provides a comprehensive breakdown of the discretization schemes that have been assigned to each term. It should be noted that the asterisks are intended to resemble the exact same term within the software:

Table 4. List of assigned discretizing schemes to each term.

Terms	Schemes
ddtSchemes	localEuler
gradSchemes	GaussLinear
div(phi,U)	Gauss limitedLinearV 1
div(phi,Yi)	Gauss limitedLinear01 1
div(phi,h)	Gauss limitedLinear 1
div(phi,k)	Gauss limitedLinear 1
div(phi,p)	Gauss limitedLinear 1
div(phi,epsilon)	Gauss limitedLinear 1
div(phi,Yi_h)	Gauss limitedLinear01 1
div(phi,k)	Gauss limitedLinear 1
div(((rho*nuEff)*dev2(T(grad(U)))))	GaussLinear
laplacianSchemes	GaussLinear orthogonal
interpolationSchemes	Linear
snGradSchemes	Orthogonal

7. Solution Procedures

The numerical test cases were modified by altering the files within the constant folder to exclude combustion and reaction phenomena, as these were not observed in the experiment. The PIMPLE algorithm was utilized to solve the governing equations by setting 1, 1, 2, and 0 to nNonOrthogonalCorrections, nOuterCorrectors, nCorrectors, and relaxationFactors, respectively.

In order to conduct a fully transient simulation of this problem, it is necessary to determine the time required for the slower fluid to traverse the entire domain. Typically, a simulation time ranging from 15 to 20 instances is adequate. The optimal time step can be established by restricting the Courant number to a range of 3 to 4, which can fluctuate based on the attributes of the problem and the trial-and-error process. This study employed a local-time stepping approach, more precisely a pseudo-transient simulation, to expedite the attainment of the steady-state state. The localEuler discretization scheme was utilized to adjust the temporal terms discretization. The variables endTime and deltaT found in the controlDict file are exclusively utilized for controlling the number of iterations and do not hold any physical significance. The fvSolution file has been modified to set the convergence level for Y_i (species) and other variables to 10×10^{-8} and 10×10^{-6} , respectively.

The system folder includes a file named sampleDict that contains essential data for x/D values of 0, 4, 15, 30, and 50, as well as for the axis boundary ($y/D = 0$). Each of these values has 101 data points. The data presented in the createGraphs directory for every test case using gnuplot were sourced from the outcomes documented by OpenFOAM in the postProcessing > sample > 30,000 directories for the final iteration of each test case. The data were exported to Microsoft Excel and graphed alongside the experimental data to facilitate comparison. Please refer to Figures 6–28, located at the conclusion of this research.

Table 5 exhibits the generation of four meshes that possess different cell sizes and aspect ratios:

Table 5. Numerical specifications of the meshes used in four test cases.

Mesh	Number of Cells	Max. Aspect Ratio	Max. Skewness	Non-Orthogonality	Converged at about (Iteration)	Needed Time (h) for 30,000 Iterations on 1 CPU
A	20,100	35.169	0.331	0	6000	1 30'
B	57,900	8.793	0.331	0	8000	4
C	115,476	8.699	0.331	0	12,000	10 45'
D	231,600	8.793	0.331	0	17,000	18

Subsequently, the test cases were executed for 30,000 iterations. The massGraph file was utilized to generate massGraph.eps for every test case, which was then used to analyze the necessary iterations for convergence [2–5]. The independent grid was selected by comparing the profile of the half radius of the velocity at $x/D = 50$ for all test cases (Figure 36). Moreover, the figures of velocity and pressure (p) are demonstrated. The performance phases of each test case were carried out in serial mode (on a single CPU) on a standard personal laptop using the Allrun script file. The precision of numerical measurements was assessed by examining convergence diagrams of mass flux and total momentum for Propane at four reference levels ($x/D = 0, 4, 15,$ and 30) for each of the four test cases. The plots presented depict the convergence, as well as the conservation of Propane and the total momentum of Propane.

Upon completion of the necessary iterations for each test case, the total mass flux of the numerical domain (partitioned into 5-degree sections) at all four reference levels has been observed to converge to 2.952×10^{-2} g/s (equivalent to 2.125 gr/s for the assumed total reference cylinder). This value represents a 7.6% reduction from the measured mass flux obtained through the flow meter and a 2.8% reduction from the mass flux measured by data extracted through the Rayleigh Scattering System and Laser Doppler Velocimetry.

8. Results and Discussions

Table 6 provides a comprehensive list of the figures that are located at the conclusion of this particular section:

Table 6. List of figures that are located at the end of this section.

Figure	Contents
Figure 2	Convergence diagram of mass flux for Mesh A
Figure 3	Convergence diagram of mass flux for Mesh B
Figure 4	Convergence diagram of mass flux for Mesh C
Figure 5	Convergence diagram of mass flux for Mesh D
Figure 6	Axial profile of mixture fraction of Propane – $y/D = 0$ (Mesh B)
Figure 7	Radial profile of mixture fraction of Propane – $x/D = 4$ (Mesh B)
Figure 8	Radial profile of mixture fraction of Propane – $x/D = 15$ (Mesh B)
Figure 9	Radial profile of mixture fraction of Propane – $x/D = 30$ (Mesh B)
Figure 10	Radial profile of mixture fraction of Propane – $x/D = 50$ (Mesh B)
Figure 11	Variations of mixture fraction half radius (L_f) with Axial Distance (Mesh B)
Figure 12	Axial profile of Turbulence Kinetic Energy (k) – $y/D = 0$ (Mesh B)
Figure 13	Radial profile of turbulence kinetic energy (k) for AIR (Hot Wire Anemometry) – $x/D = 0$ (Mesh B)
Figure 14	Radial profile of turbulence kinetic energy (k) – $x/D = 4$ (Mesh B)
Figure 15	Radial profile of turbulence kinetic energy (k) – $x/D = 15$ (Mesh B)
Figure 16	Radial profile of turbulence kinetic energy (k) – $x/D = 30$ (Mesh B)
Figure 17	Radial profile of turbulence kinetic energy (k) – $x/D = 50$ (Mesh B)
Figure 18	Axial profile of U_{mean} – $y/D = 0$ (Mesh B)
Figure 19	Radial profile of U_{mean} for AIR (Hot Wire Anemometry) – $x/D = 0$ (Mesh B)
Figure 20	Radial profile of U_{mean} – $x/D = 4$ (Mesh B)
Figure 21	Radial profile of U_{mean} – $x/D = 15$ (Mesh B)
Figure 22	Radial profile of U_{mean} – $x/D = 30$ (Mesh B)
Figure 23	Radial profile of U_{mean} – $x/D = 50$ (Mesh B)
Figure 24	Axial profile of V_{mean} – $y/D = 0$ (Mesh B)
Figure 25	Radial profile of V_{mean} – $x/D = 4$ (Mesh B)
Figure 26	Radial profile of V_{mean} – $x/D = 15$ (Mesh B)
Figure 27	Radial profile of V_{mean} – $x/D = 30$ (Mesh B)
Figure 28	Radial profile of V_{mean} – $x/D = 50$ (Mesh B)
Figure 29	Schematic domain
Figure 30	Schematic Mesh
Figure 31	Schematic Mesh B
Figure 32	Pressure (Mesh B)
Figure 33	Velocity (Mesh B)
Figure 34	Velocity (Mesh B)
Figure 35	Velocity (Mesh B)
Figure 36	Mesh independency comparison for a half radius of the velocity profile at $x/D = 50$

8.1. U_{mean}

The U_{mean} values exhibit stability for approximately six jet diameters downstream of the nozzle outlet. Subsequently, it experiences a rapid decline and converges with the velocity of the outer co-flowing air, which is 9.2 m/s, at a further downstream distance. The phenomenon of mixing between injected Propane and co-flowing air is predominantly attributed to turbulence generated by vortices. It is imperative to highlight this aspect.

The vorticity transport equation features a source term that is contingent upon the mean velocity gradient. The increase in velocity gradients results in a corresponding increase in the intensification of vorticities, turbulence, and mixing.

The numerical U_{mean} 's radial profiles are shown in Figures 18–23. These figures demonstrate that the profile agrees well with the experimental data in the region of the jet, specifically for x/D values less than 10. The conformity of the flow gradually decreases towards the outlet, particularly within the range of $10 < x/D < 30$. At x/D values greater than 30, this phenomenon will undergo a revitalization and substantial enhancement. Normalization of radial distance, y , by the inner diameter of the nozzle, D , is a crucial consideration.

Figures 20–23 depicting the numerical mean radial profiles of U_{mean} indicate that the mean velocities tend to approach the free stream value of 9.2 m/s as the radial distance increases. However, the rate of approach is comparatively slower. The velocity behavior exhibits similarity to the mixed fraction behavior of Propane, as depicted in Figure 6 of L_f 's diagram. The width of the jet will gradually increase as it moves away from the nozzle.

Figure 19 displays the radial profile of U_{mean} at $x/D = 0$. The results obtained from numerical simulations and experimental data exhibit satisfactory conformity, especially from the nozzle's outer diameter ($y/D = 1.7$) towards the left boundary.

8.2. V_{mean}

Figures 25–28 illustrate that V_{mean} corresponds numerically to the experimental results of both AIR and JET seeding. Moving closer to the power source can reduce the degree of compliance. Unfortunately, it is not possible to attain a logical coincidence between the numerical and experimental outcomes in the axial profile of V_{mean} at $y/D = 0$, as depicted in Figure 24.

The issue at hand may be attributed to the limitations of all Reynolds-Averaged Navier-Stokes (RANS) models, which involve numerous simplified assumptions, or the oversimplification of the numerical model used in this study. Specifically, the treatment of the effect of the wall boundaries may have contributed to this issue. The acquisition of radial velocity (V_{mean}) may prove to be a difficult task, despite the utilization of sophisticated models, such as Detached Eddy Simulation (DES), Large Eddy Simulation (LES), Direct Numerical Simulation (DNS), and their diverse variants [26].

8.3. Turbulence Kinetic Energy (k)

The radial profiles of Turbulence Kinetic Energy (k) depicted in Figures 12 and 14–17 exhibit conformity with the experimental data. As the velocity fluctuations decrease (i.e., x/D exceeds 50), conformity improves when approaching the outlet.

Figures 14–17 display the numerical mean radial profiles of k . These figures indicate that there is a gradual reduction in turbulence kinetic energy (k) as the radial distance increases. The expansion of jet width gradually occurs after the nozzle, which is in line with the depiction of the Mixed Fraction of Propane in Figure 6 of L_f 's diagram. This phenomenon is similar to U_{mean} .

Figure 13 displays the radial profile of turbulence kinetic energy (k) at $x/D = 0$. The results obtained from numerical simulations and experimental data exhibit satisfactory conformity, especially in the region extending from the outer diameter of the nozzle ($y/D = 1.7$) to the left boundary. The present item bears a resemblance to the U_{mean} profile.

8.4. Mixture Fraction of Propane

Experimental data for the mean mixture fraction of Propane at the inlet ($x/d = 0$) could not be obtained due to technical issues encountered during the corresponding experiments. Axial and radial comparisons were conducted at four different locations, namely $x/D = 4, 15, 30, \text{ and } 50$, as shown in Figures 6–11.

The findings indicate a significant concurrence between the numerical and experimental data concerning the average mixture fraction and its half radius (L_f) in both axial

and radial profiles. The numerical results show that at $x/D = 4$, the mean mixture fraction values of unity, which correspond to pure Propane, suggest the presence of a potential core that extends around 0.2 diameters from the centerline. The potential core region, which spans almost six times the jet diameters downstream of the nozzle's outlet, maintains a relatively constant numerical mean mixture fraction. However, beyond this region, the mixture fraction experiences a sharp decline. This decline is attributed to the entrainment of co-flowing air, which is caused by Kelvin–Helmholtz instabilities resulting from the significant difference between the velocity of the jet and the velocity of air.

The results of the numerical simulations indicate that the total mass flux within the 5-degree sector of the numerical domain has reached a convergence value of 2.9528×10^{-2} g/s, following an adequate number of iterations in each test case. The value obtained is 7.6% less than the mass flux determined by the flow meter and 2.8% less than the mass flux obtained through the Rayleigh Scattering System and Laser Doppler Velocimetry.

8.5. Mixture Fraction Half Radius (L_f)

This study utilized the mixture fraction half radius, L_f , as a means to evaluate the rate of jet spreading in a turbulent Propane jet flow that was not undergoing any chemical reactions. The parameter L_f plays a crucial role in determining the mixing behavior of a Propane jet flow. The half-value radius is a technical term that refers to the distance from the centerline of a jet where the mixture fraction is equivalent to half of its value at the centerline. Normalization of L_f by the jet diameter, D , was executed to enable convenient comparison with the experimental data.

Figure 11 depicts the results of a numerical simulation, which demonstrates a noteworthy correlation with the experimental data in terms of the changes in the mixture fraction half radius, L_f , across axial distance. The Propane jet flow's turbulent behavior was effectively captured by the two-equation Realizable k - ϵ eddy viscosity turbulence model.

9. Conclusions

The objective of this study was to perform numerical simulations of velocity and mixture fraction fields in a turbulent non-reaction Propane jet flow. The jet flow was introduced into parallel co-flowing air under isothermal conditions. The objective of the research was to conduct a comparison between the numerical outcomes and experimental data acquired from a prior experimental study in Sandia Laboratory (Sandia National Laboratories, California—P.O. Box 969—Livermore, CA 94551-0969, USA): <http://www.sandia.gov/TNF/DataArch/ProJet.html> (accessed on 10 March 2023).

The objective was accomplished by meticulously modifying the reactingFoam solver, which is a standard solver in OpenFOAM, using the swak4Foam utility to eliminate reaction and combustion.

The turbulent flow field on a nearly 2D plane, specifically on a 5-degree sector of the experimental domain, was simulated using a two-equation Realizable k - ϵ eddy viscosity turbulence model. The aim of this methodology was to enhance comprehension of the flow structure and mixing mechanism in a scenario devoid of chemical interaction and heat transfer. The study compared numerical results to experimental data by analyzing numerical axial and radial profiles of mean velocities, turbulence energy, mean *mixture fraction*, and *mixture fraction half radius* (L_f).

The study demonstrated excellent agreement between the mixture fraction fields and mixture fraction half radius (L_f) obtained from simulations and those obtained from experimental data. Furthermore, it was noted that U_{mean} displayed suitable adjustments, particularly in regions where the examined areas were angled towards the nozzle exit, unlike V_{mean} . The numerical results showed precise and conforming outcomes with experimental data in the mentioned areas, despite the simplifying assumptions made in various adjustments and turbulence models.

The study emphasizes the efficacy of the two-equation Realizable k - ϵ eddy viscosity turbulence model in minimizing computational costs when compared with more advanced

turbulence models, such as Launder, Reece, and Rodi Full Reynolds Stress Model (LRR), Speziale, Sarkar, and Gatski (SSG), Detached Eddy Simulation (DES), Large Eddy Simulation (LES), Direct Numerical Simulation (DNS) and their diverse variants. This study's numerical findings indicate that the approach utilized can accurately predict turbulent non-reaction flows with minimal computational expenses.

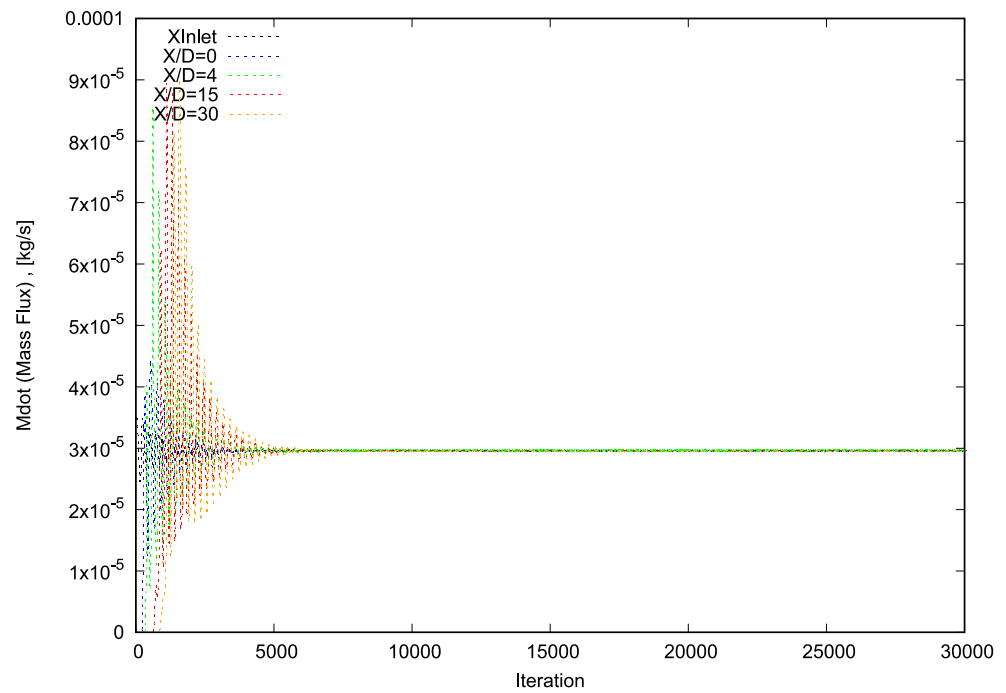


Figure 2. Convergence diagram of mass flux for Mesh A.

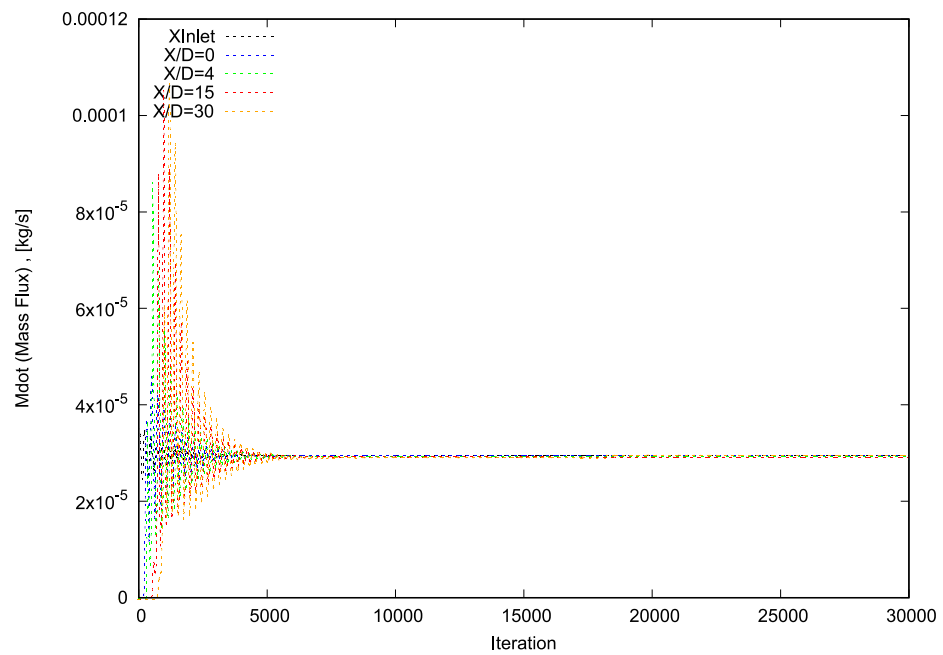


Figure 3. Convergence diagram of mass flux for Mesh B.

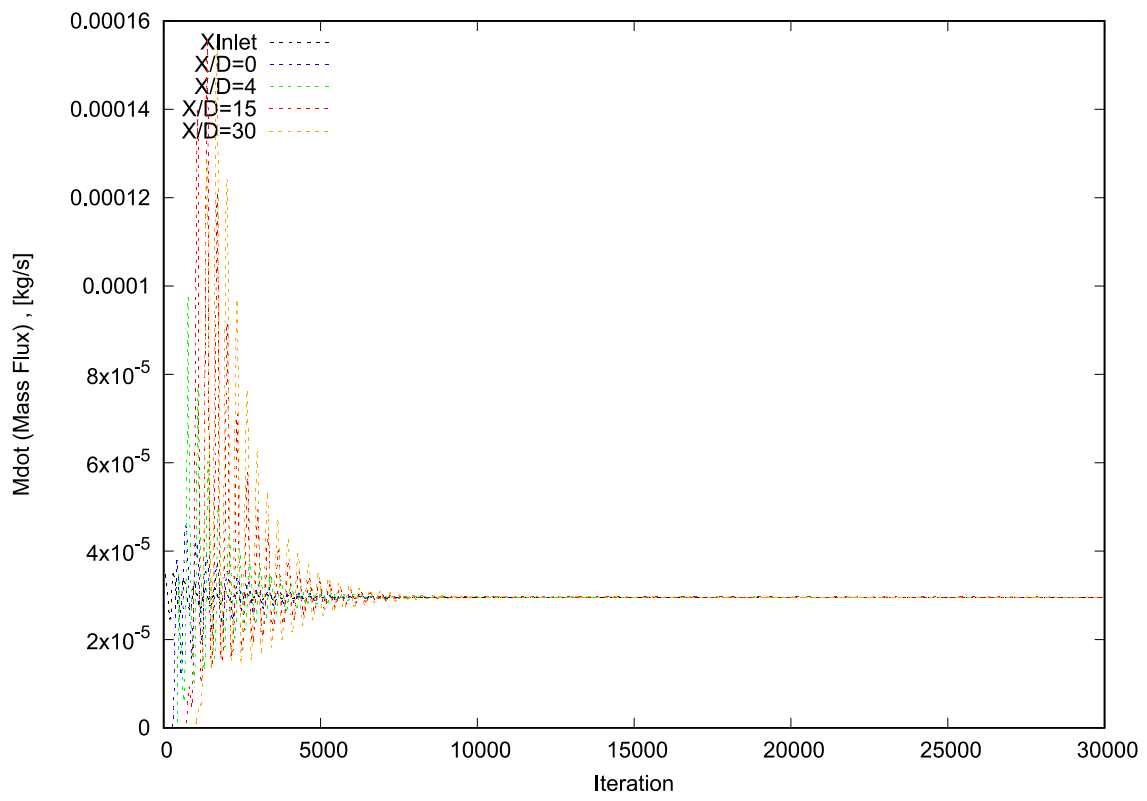


Figure 4. Convergence diagram of mass flux for Mesh C.

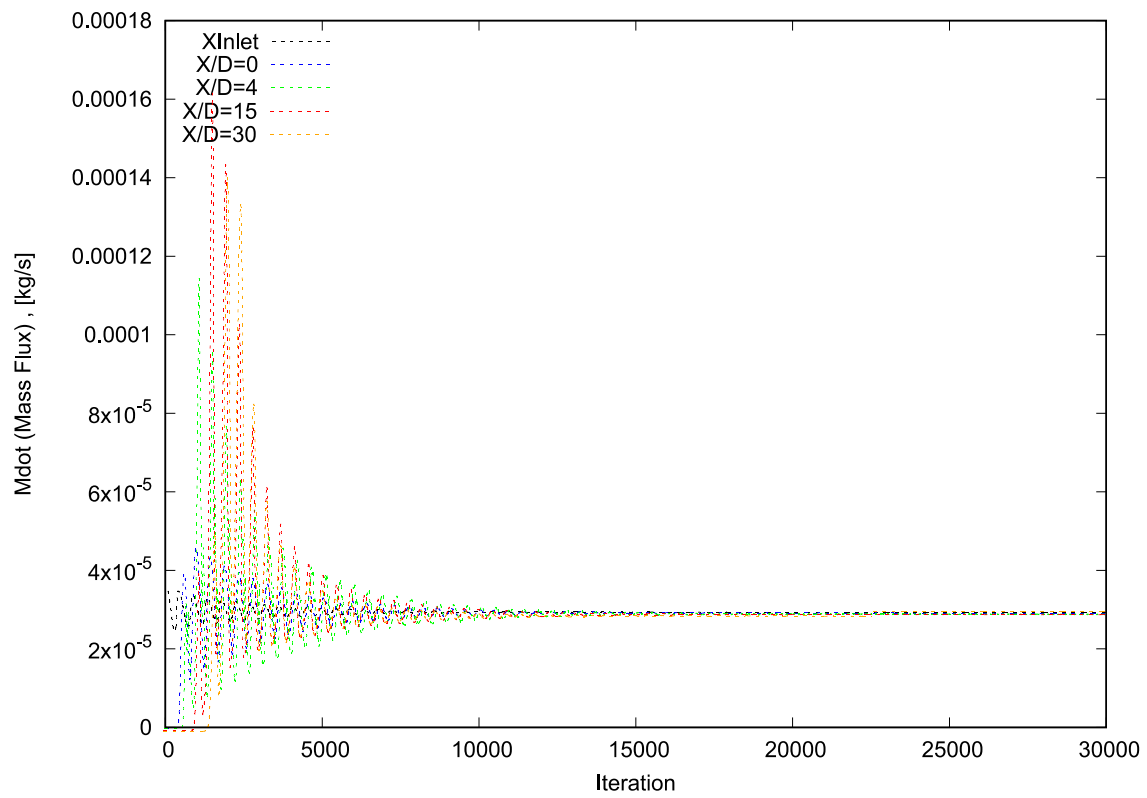


Figure 5. Convergence diagram of mass flux for Mesh D.

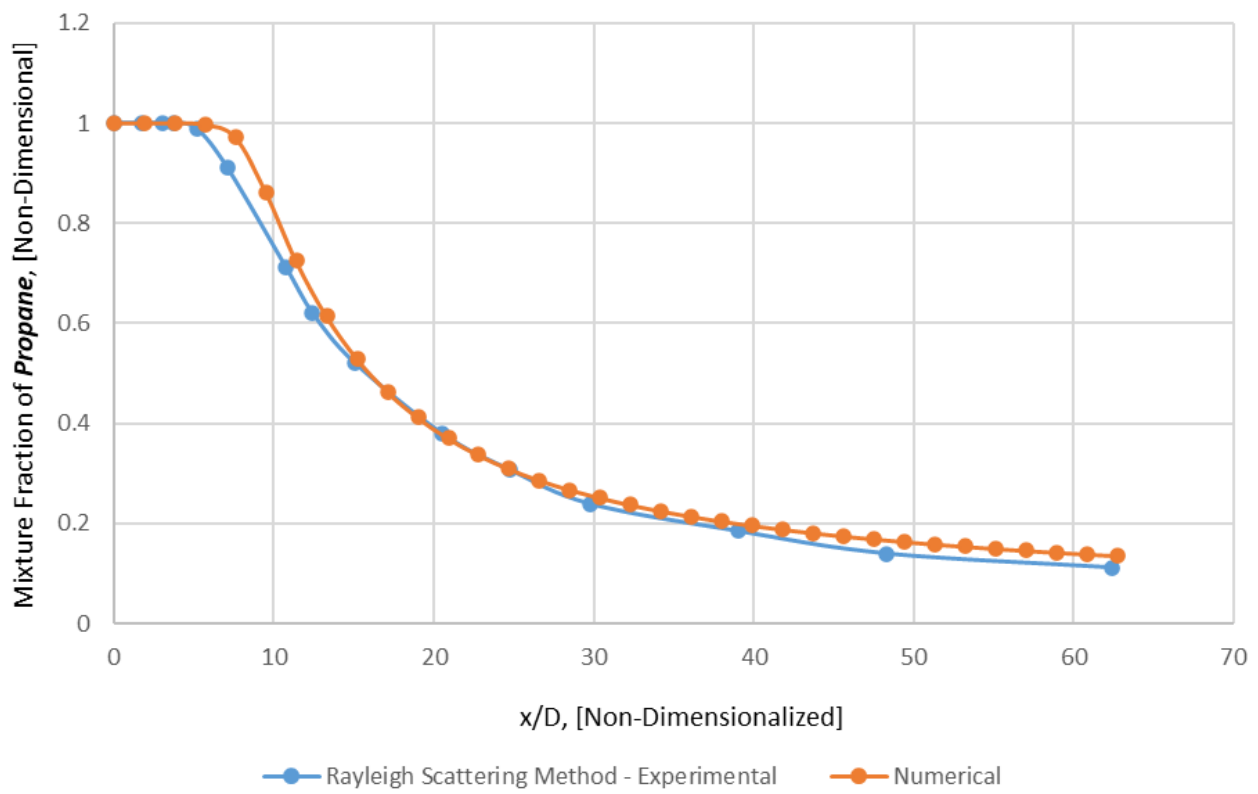


Figure 6. Axial Profile of mixture fraction of Propane – $y/D = 0$ (Mesh B).

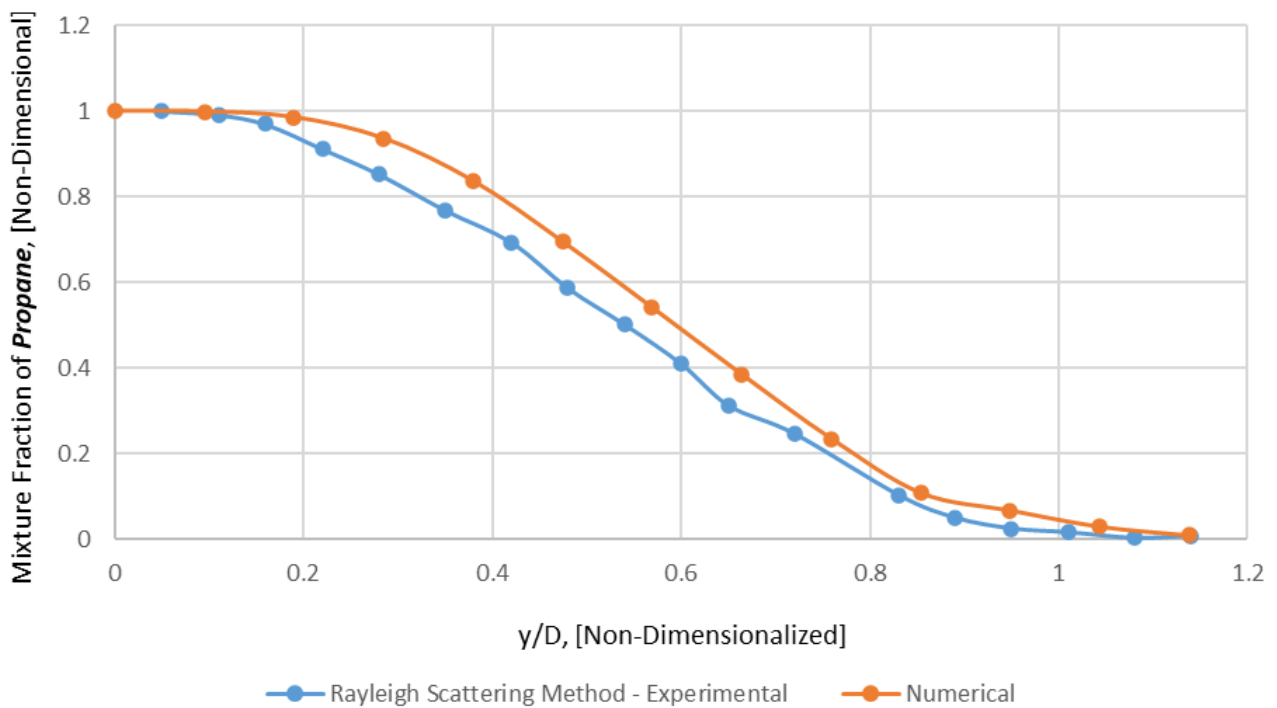


Figure 7. Radial profile of mixture fraction of Propane – $x/D = 4$ (Mesh B).

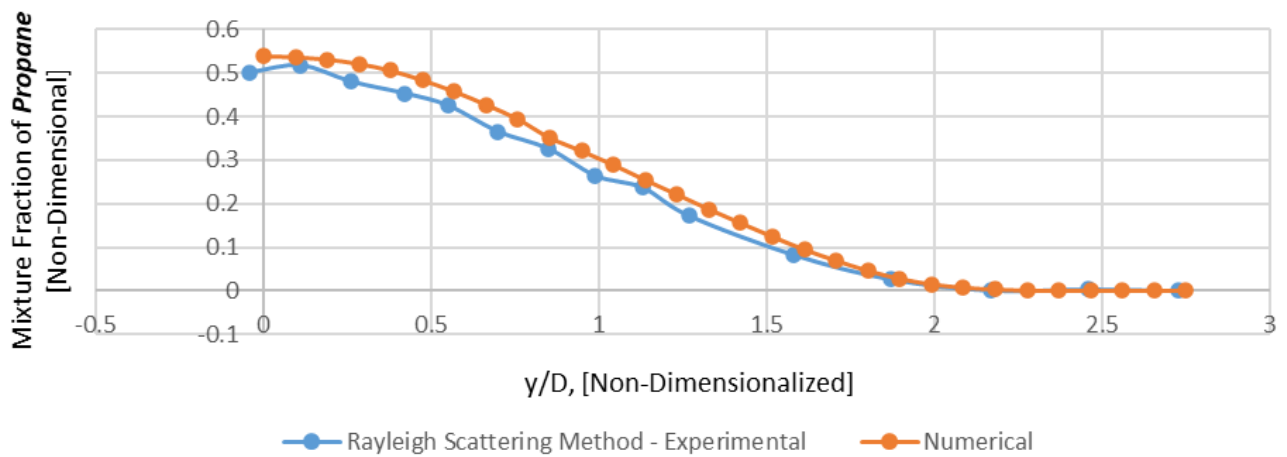


Figure 8. Radial Profile of mixture fraction of Propane – $x/D = 15$ (Mesh B).

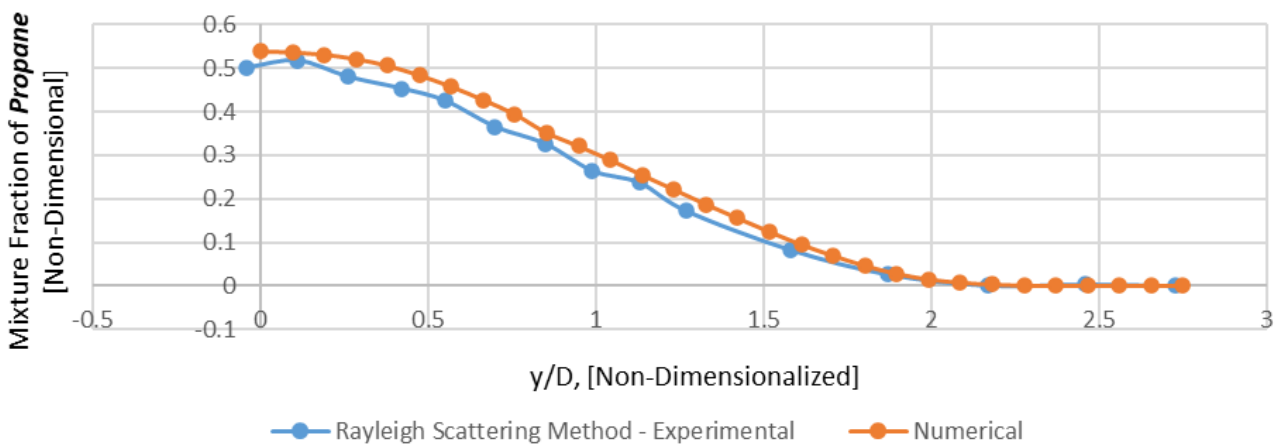


Figure 9. Radial Profile of mixture fraction of Propane – $x/D = 30$ (Mesh B).

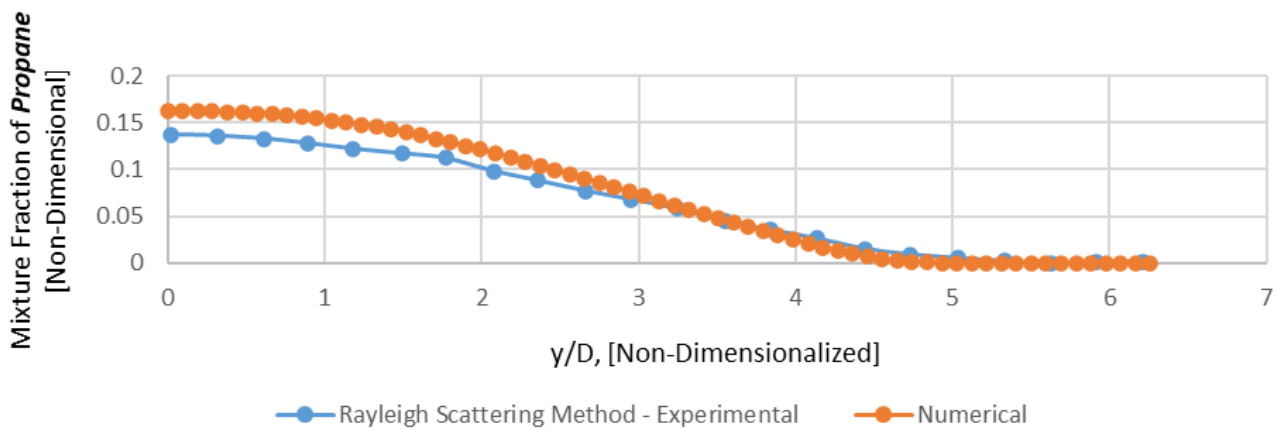


Figure 10. Radial Profile of mixture fraction of Propane – $x/D = 50$ (Mesh B).

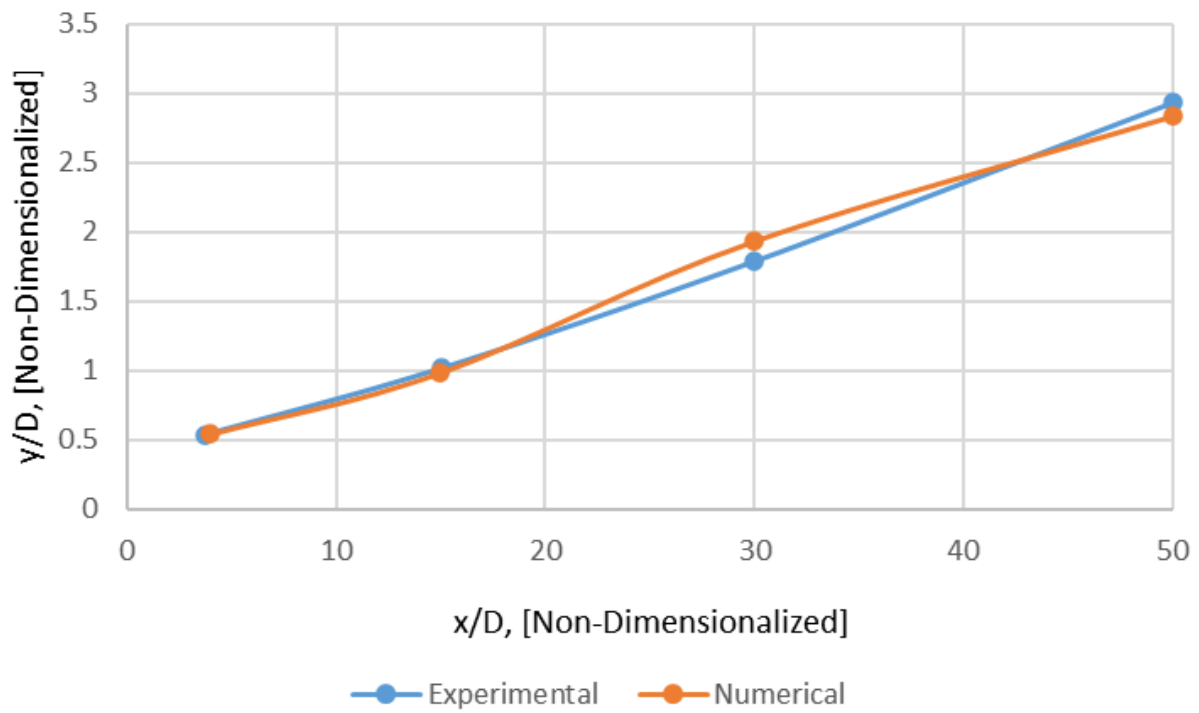


Figure 11. Variations of mixture fraction half radius (L_f) with axial distance (Mesh B).

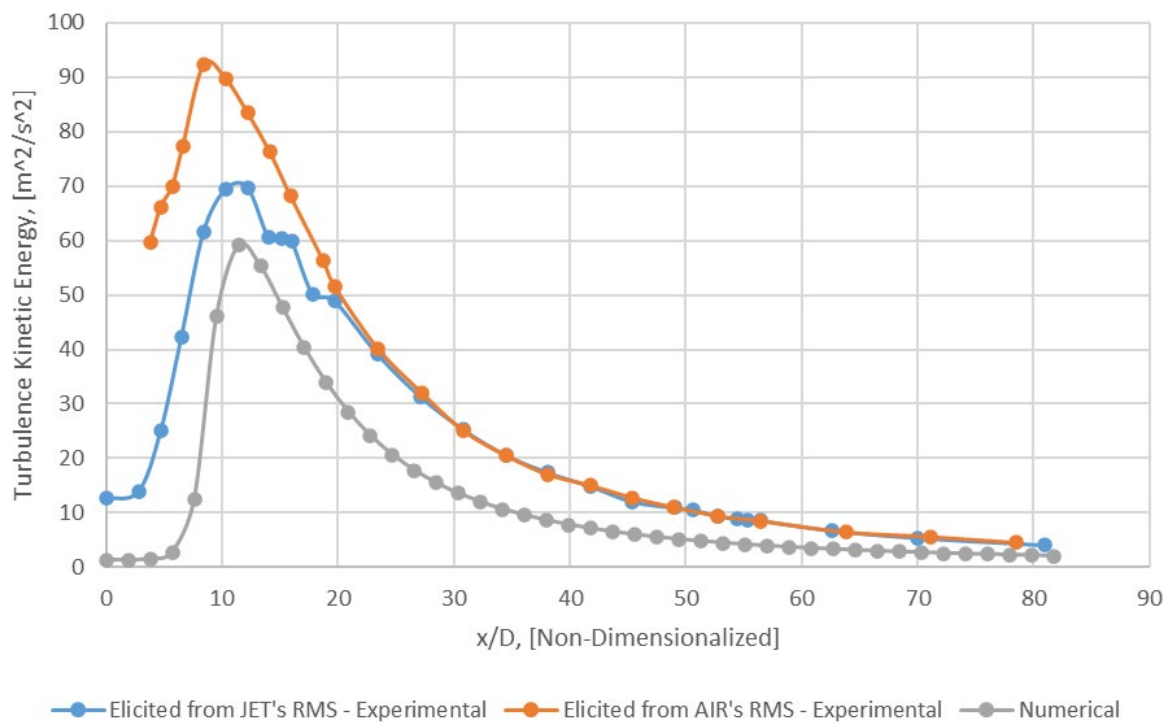


Figure 12. Axial profile of turbulence kinetic energy (k) – $y/D = 0$ (Mesh B).

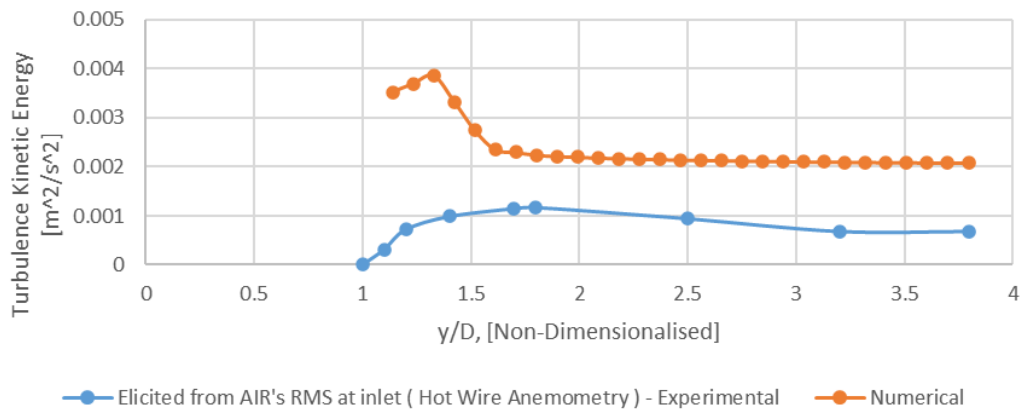


Figure 13. Radial profile of turbulence Kinetic energy (k) for AIR (Hot Wire Anemometry) – $x/D = 0$ (Mesh B).

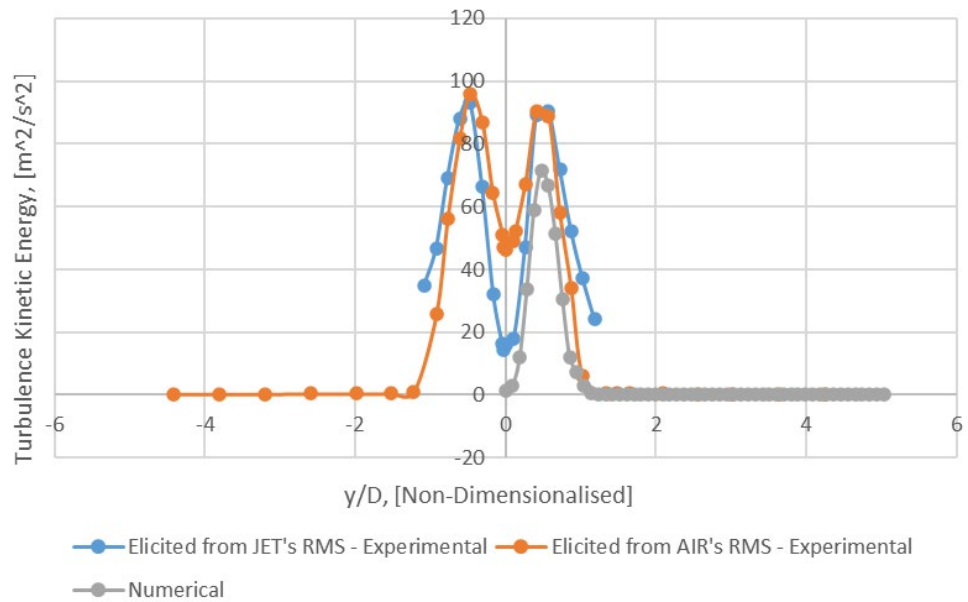


Figure 14. Radial profile of turbulence kinetic energy (k) – $x/D = 4$ (Mesh B).

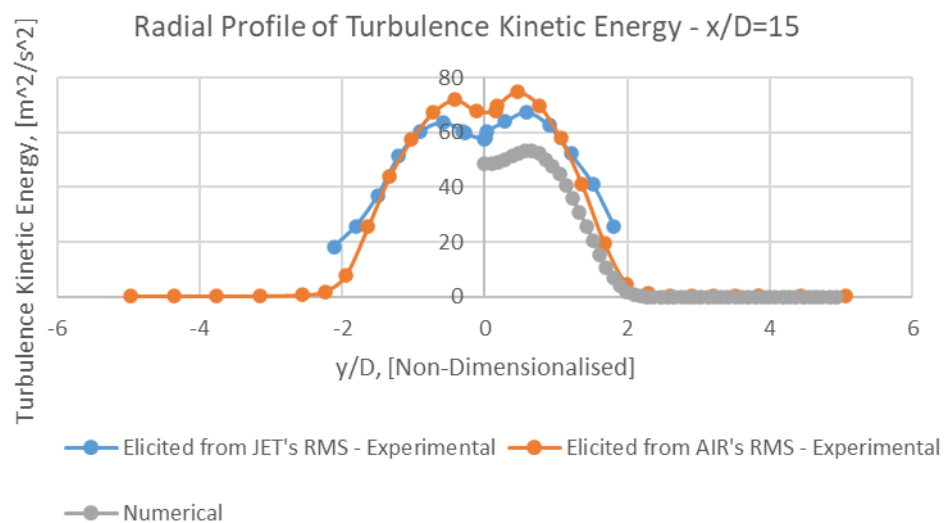


Figure 15. Radial profile of turbulence kinetic energy (k) – $x/D = 15$ (Mesh B).

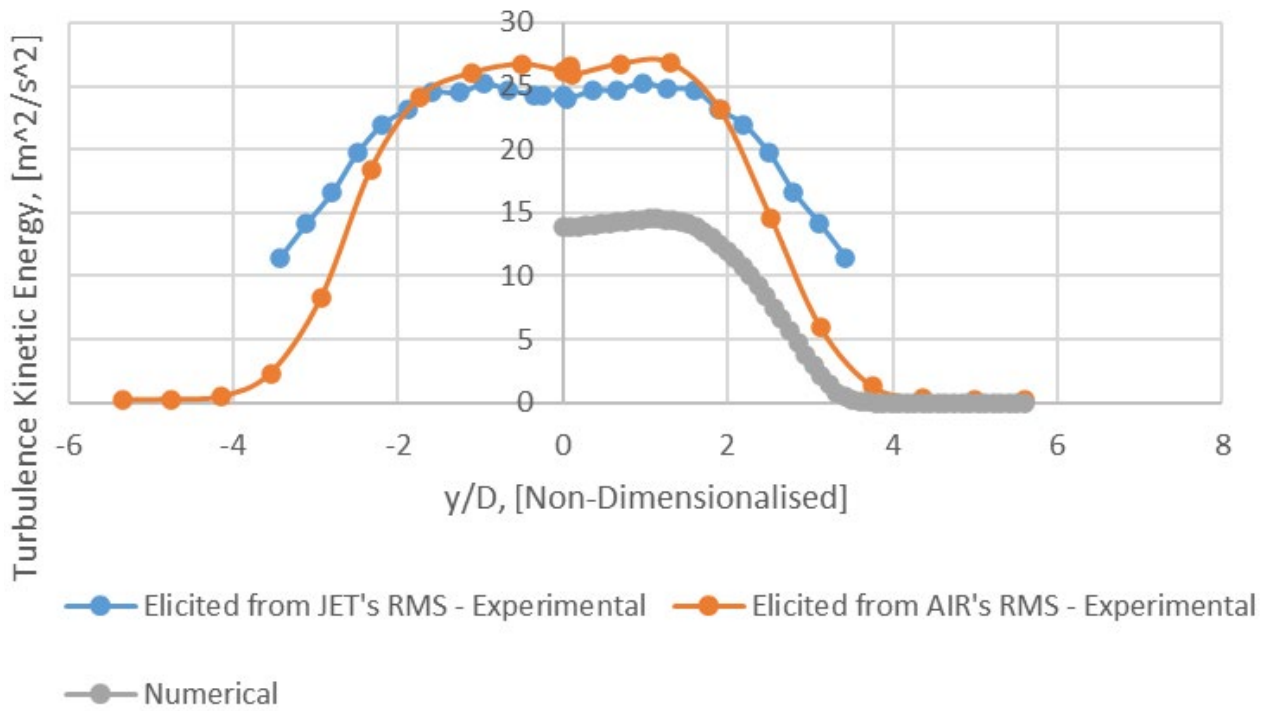


Figure 16. Radial profile of turbulence kinetic energy (k) – $x/D = 30$ (Mesh B).

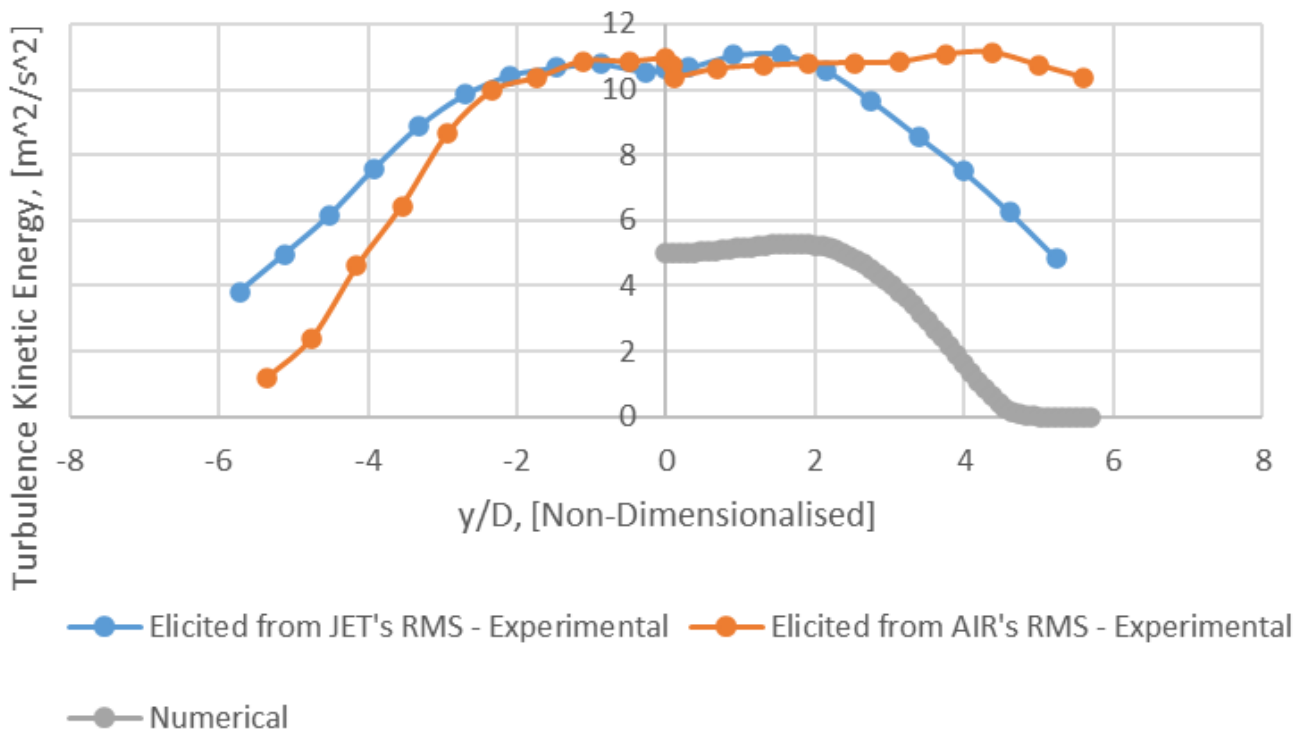


Figure 17. Radial profile of turbulence kinetic energy (k) – $x/D = 50$ (Mesh B).

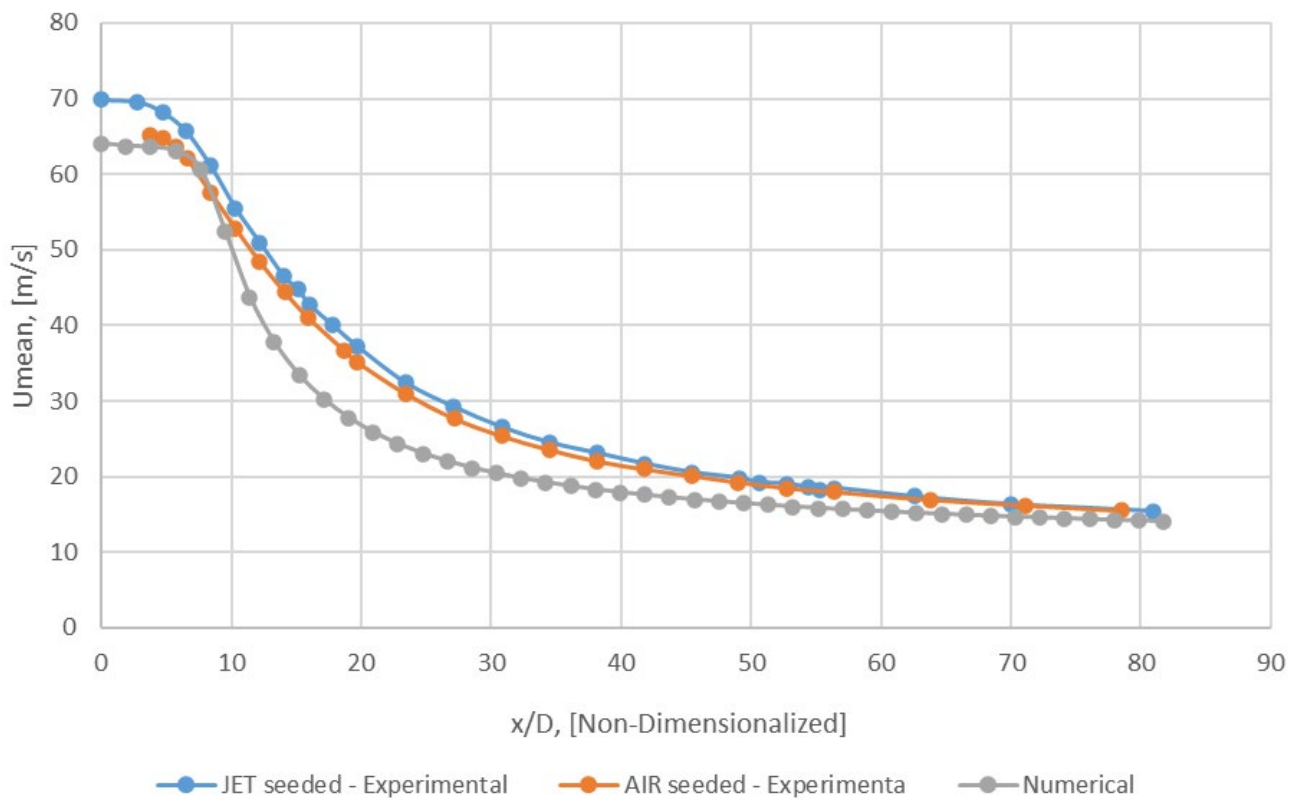


Figure 18. Axial Profile of $U_{mean} - y/D = 0$ (Mesh B).

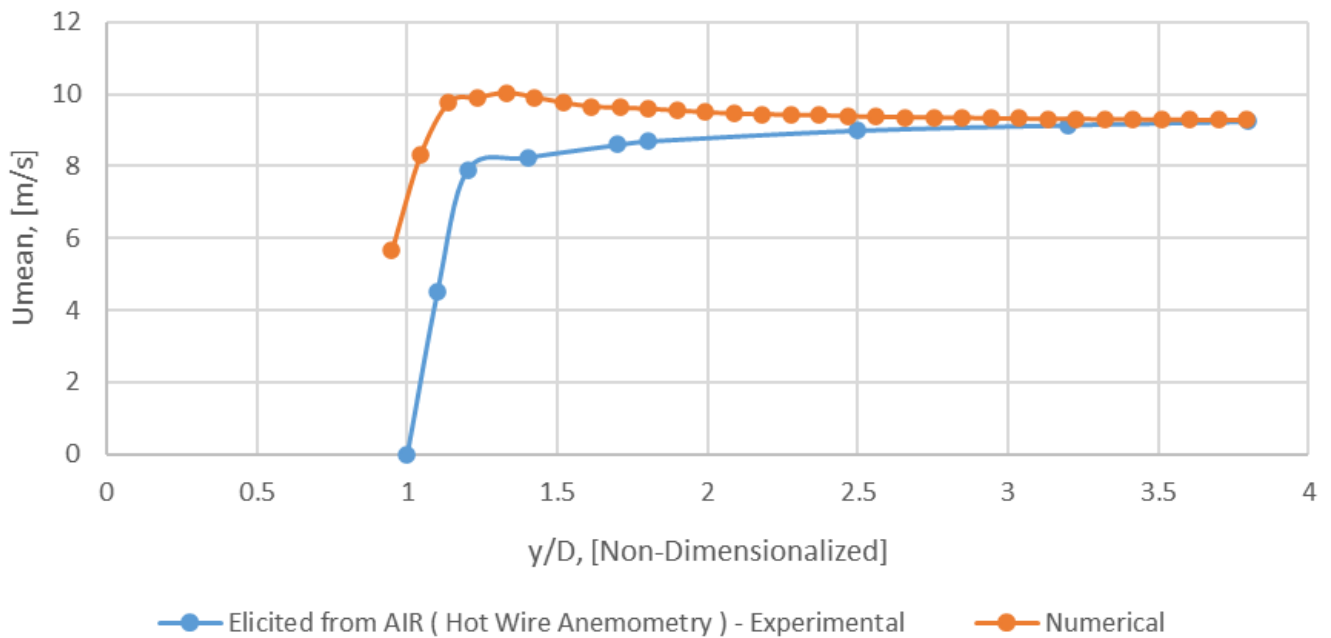


Figure 19. Radial profile of U_{mean} for AIR (Hot Wire Anemometry) - $x/D = 0$ (Mesh B).

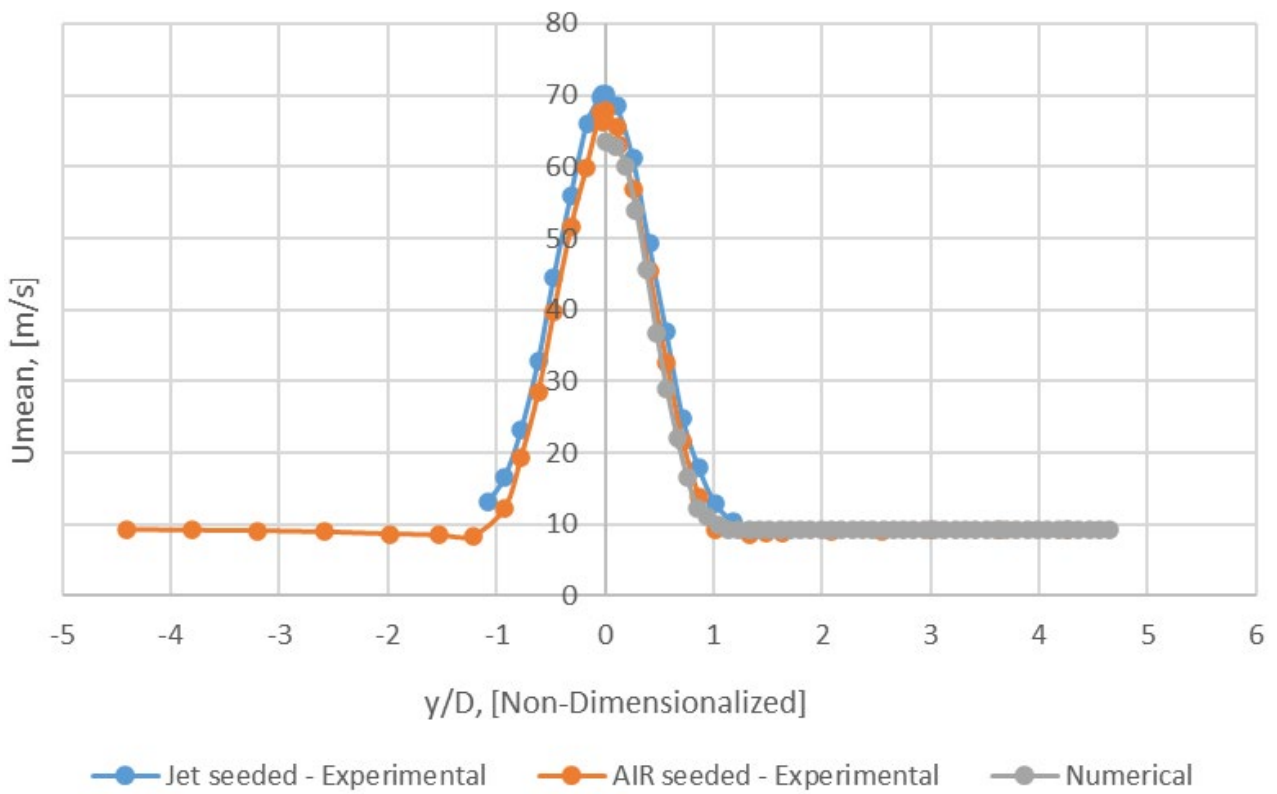


Figure 20. Radial profile of $U_{\text{mean}} - x/D = 4$ (Mesh B).

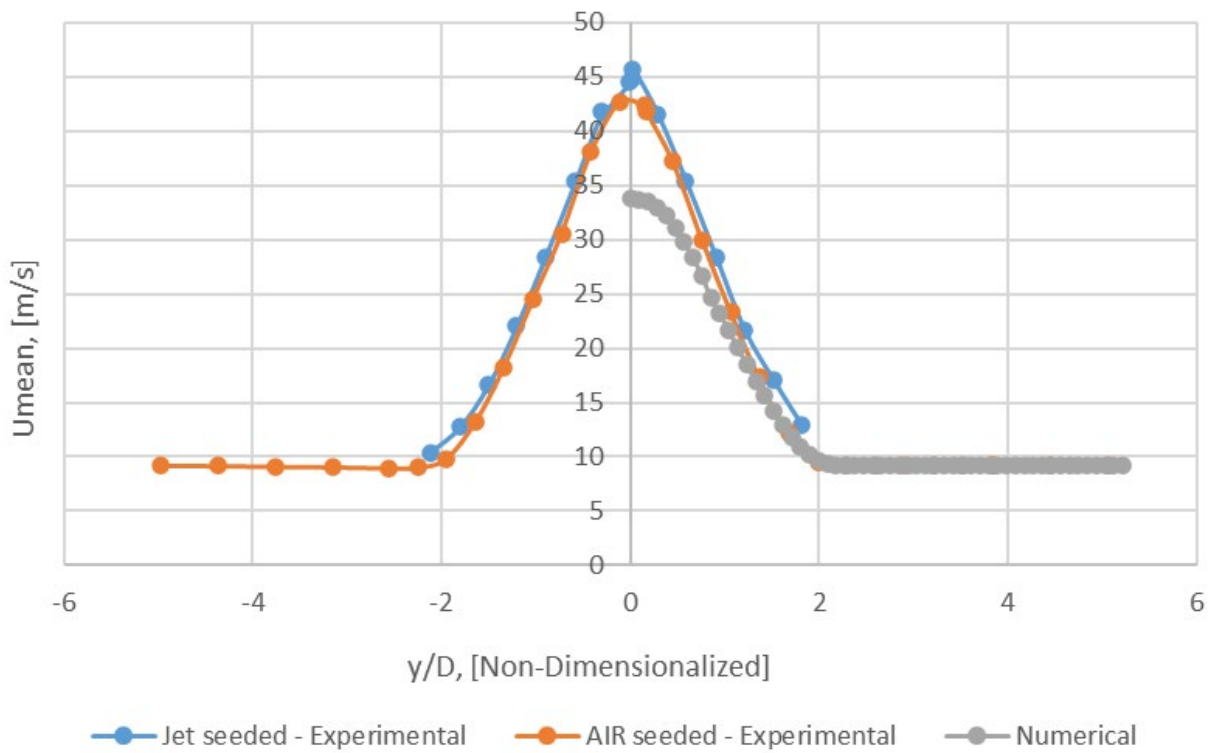


Figure 21. Radial profile of $U_{\text{mean}} - x/D = 15$ (Mesh B).

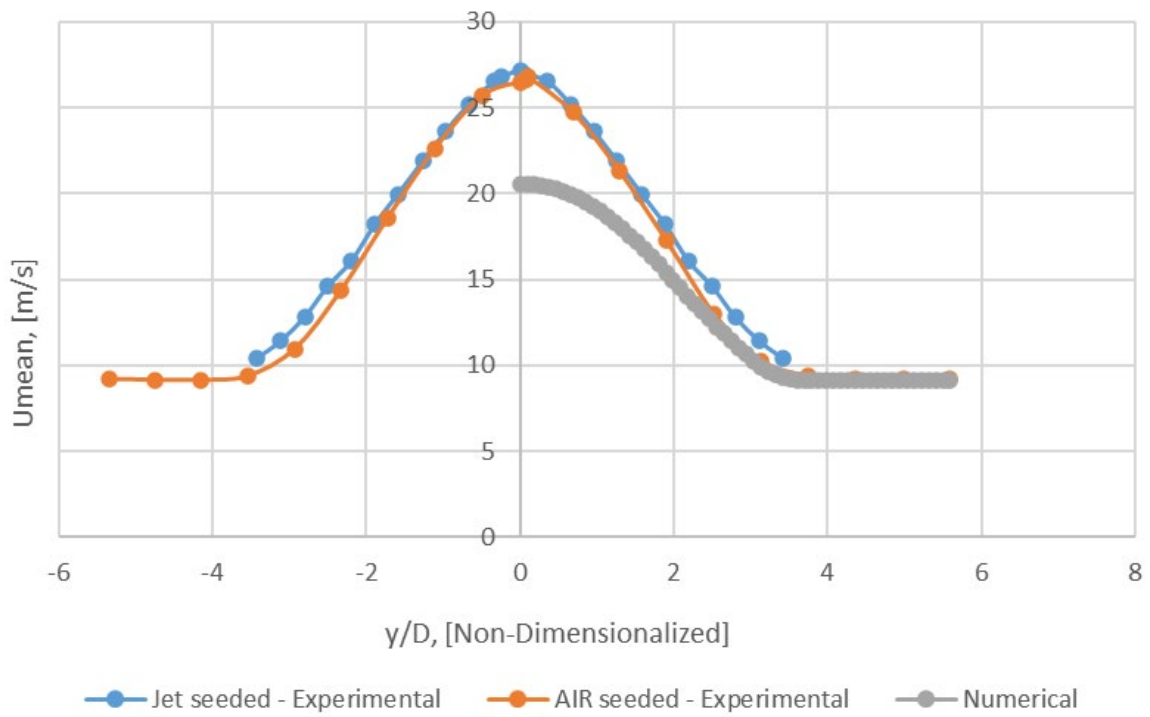


Figure 22. Radial profile of $U_{\text{mean}} - x/D = 30$ (Mesh B).

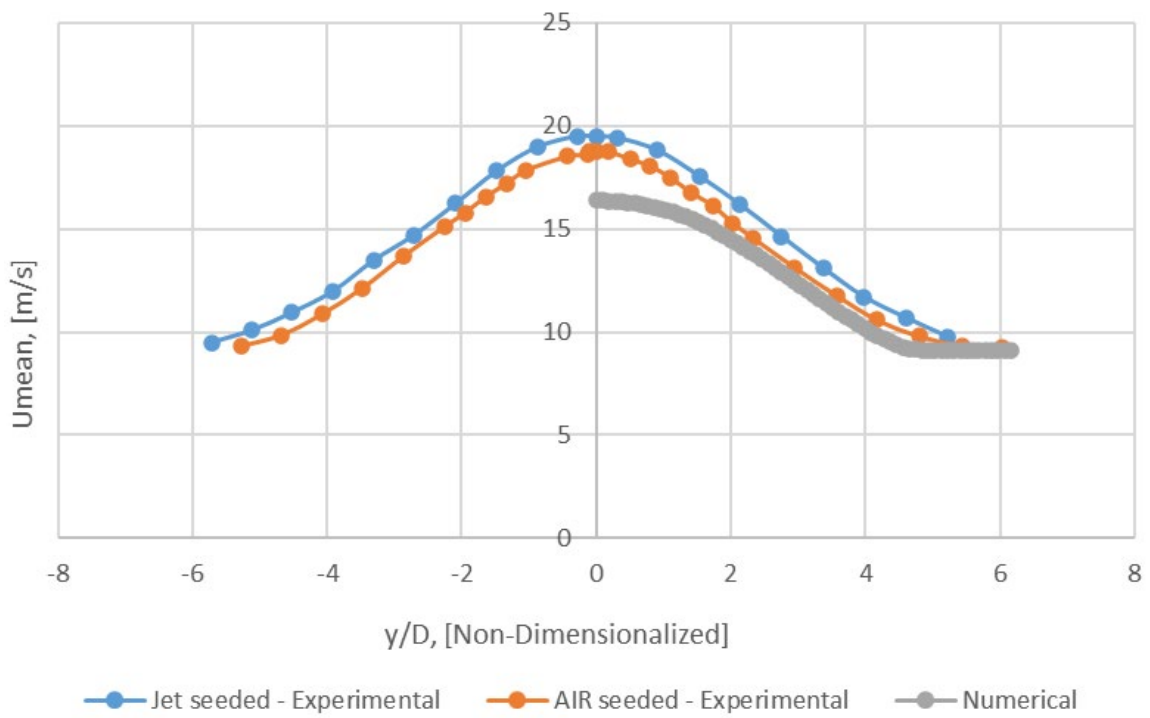


Figure 23. Radial profile of $U_{\text{mean}} - x/D = 50$ (Mesh B).

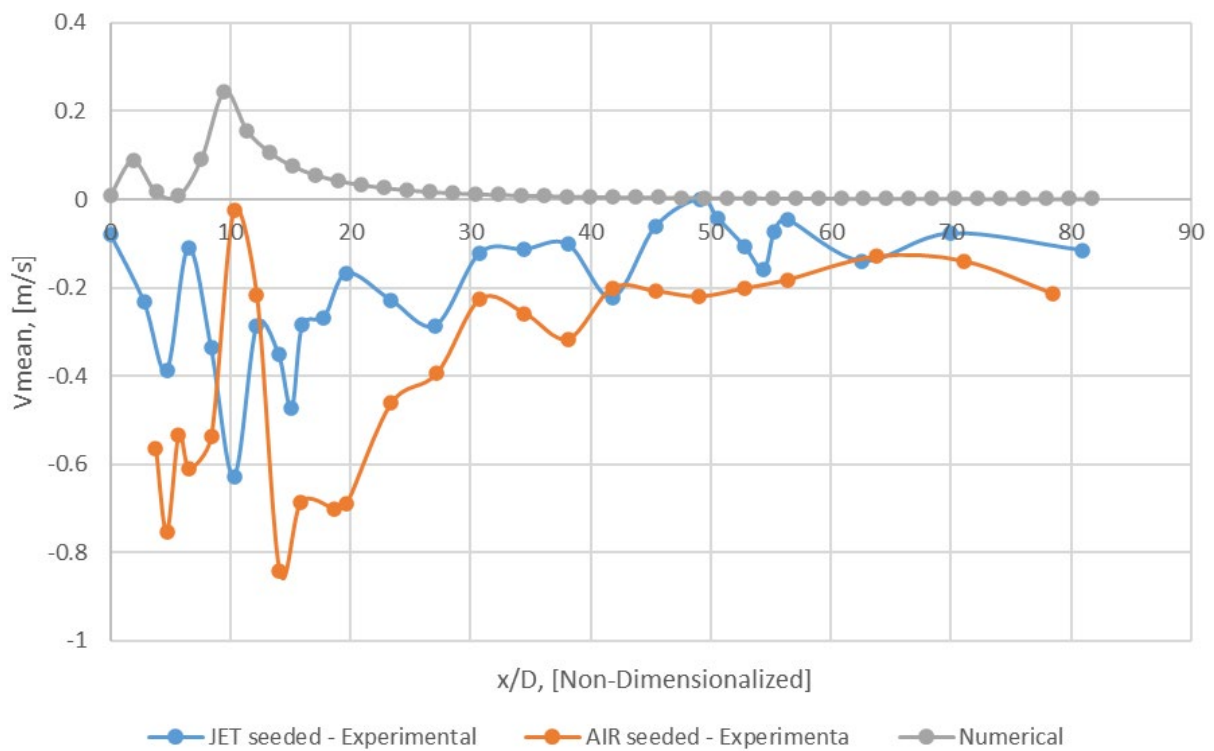


Figure 24. Axial profile of $V_{mean} - y/D = 0$ (Mesh B).

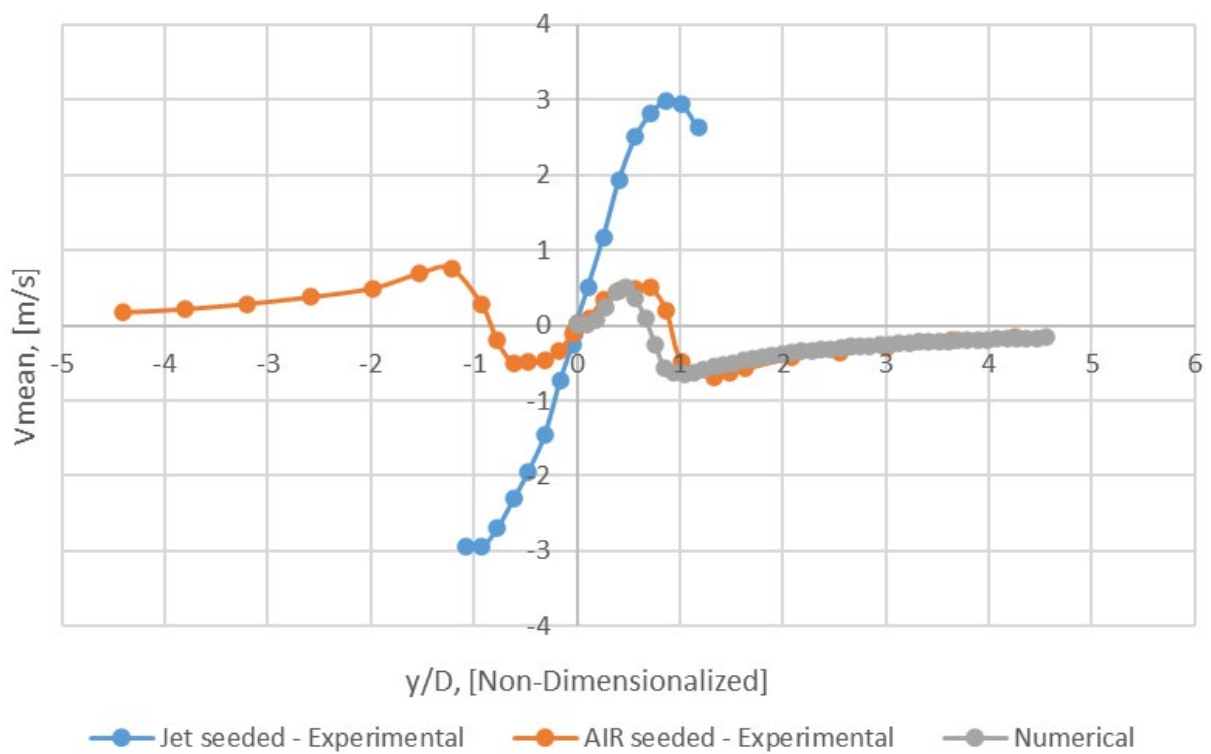


Figure 25. Radial profile of $V_{mean} - x/D = 4$ (Mesh B).

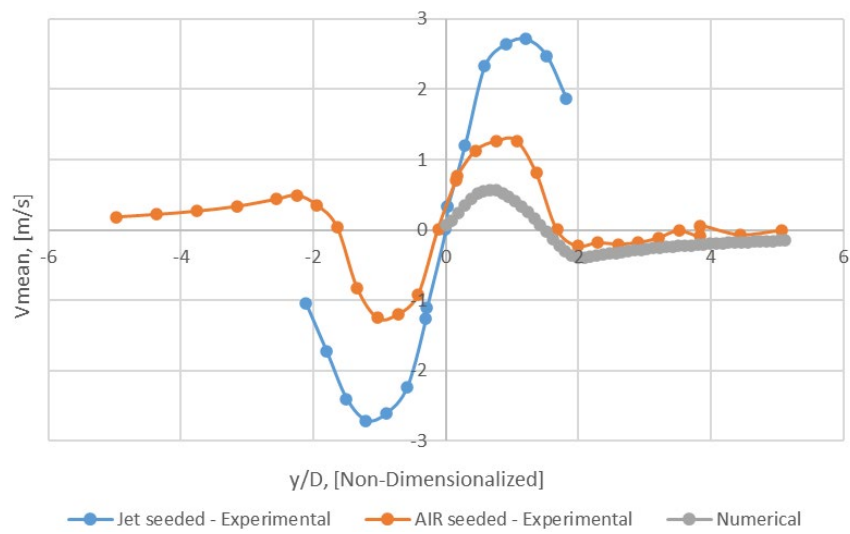


Figure 26. Radial profile of $V_{\text{mean}} - x/D = 15$ (Mesh B).

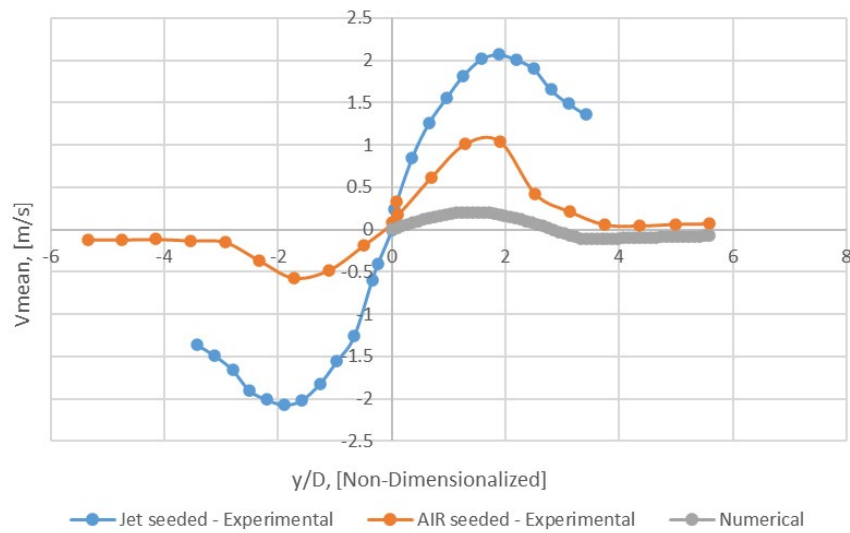


Figure 27. Radial profile of $V_{\text{mean}} - x/D = 30$ (Mesh B).

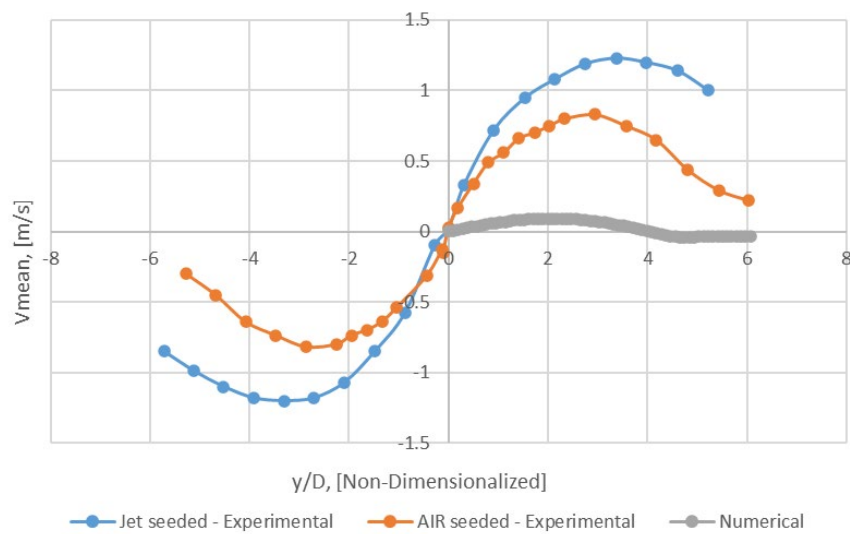


Figure 28. Radial profile of $V_{\text{mean}} - x/D = 50$ (Mesh B).

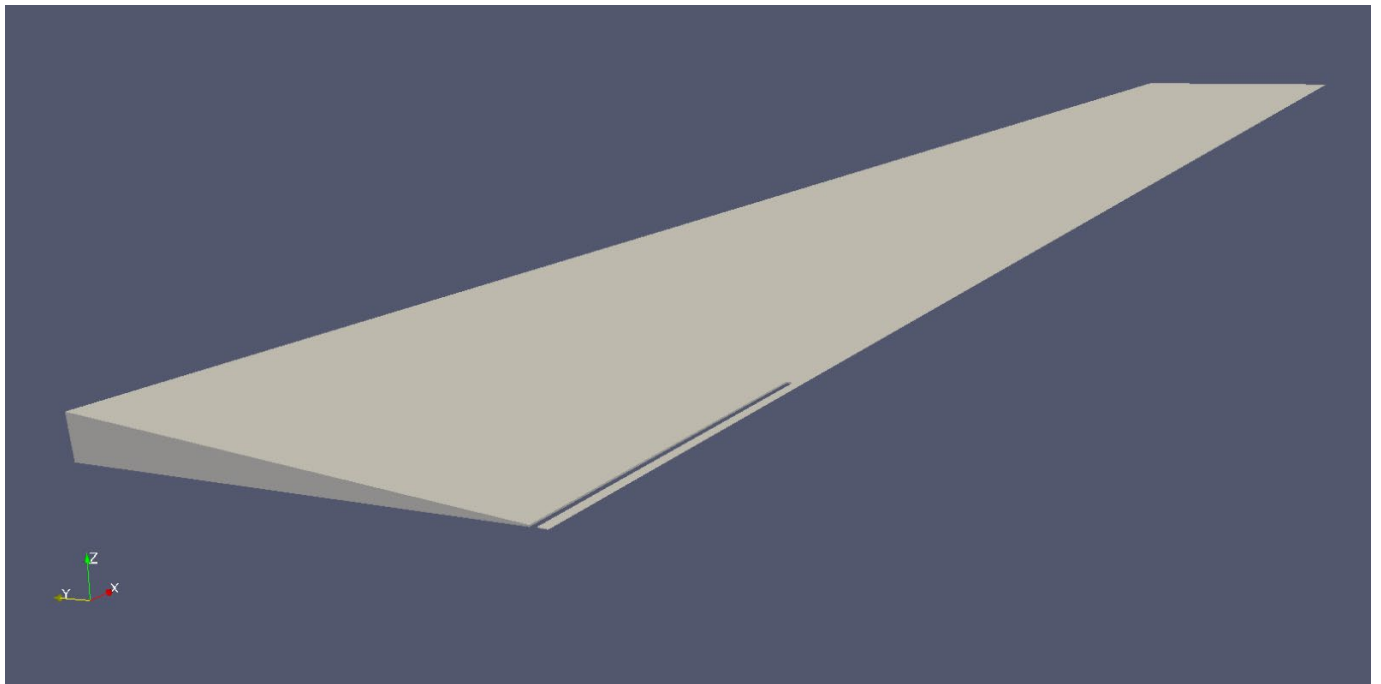


Figure 29. Schematic domain B.

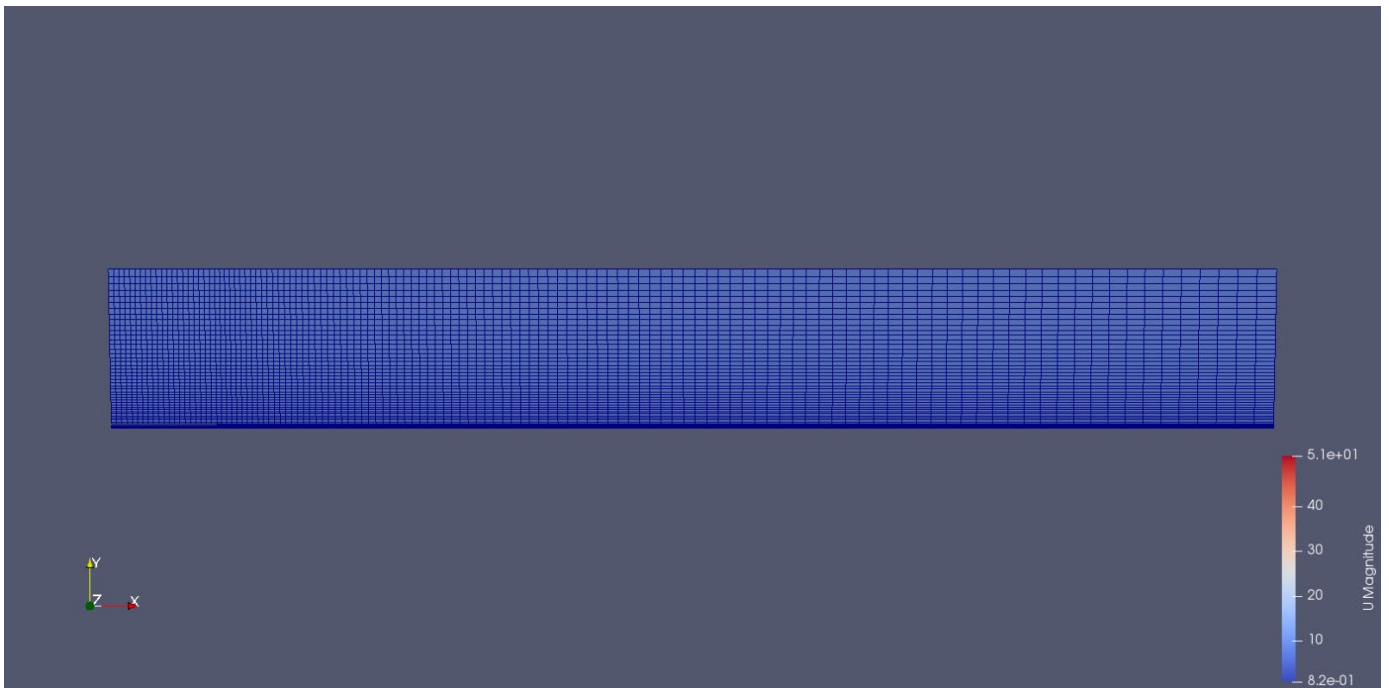


Figure 30. Schematic of a mesh.

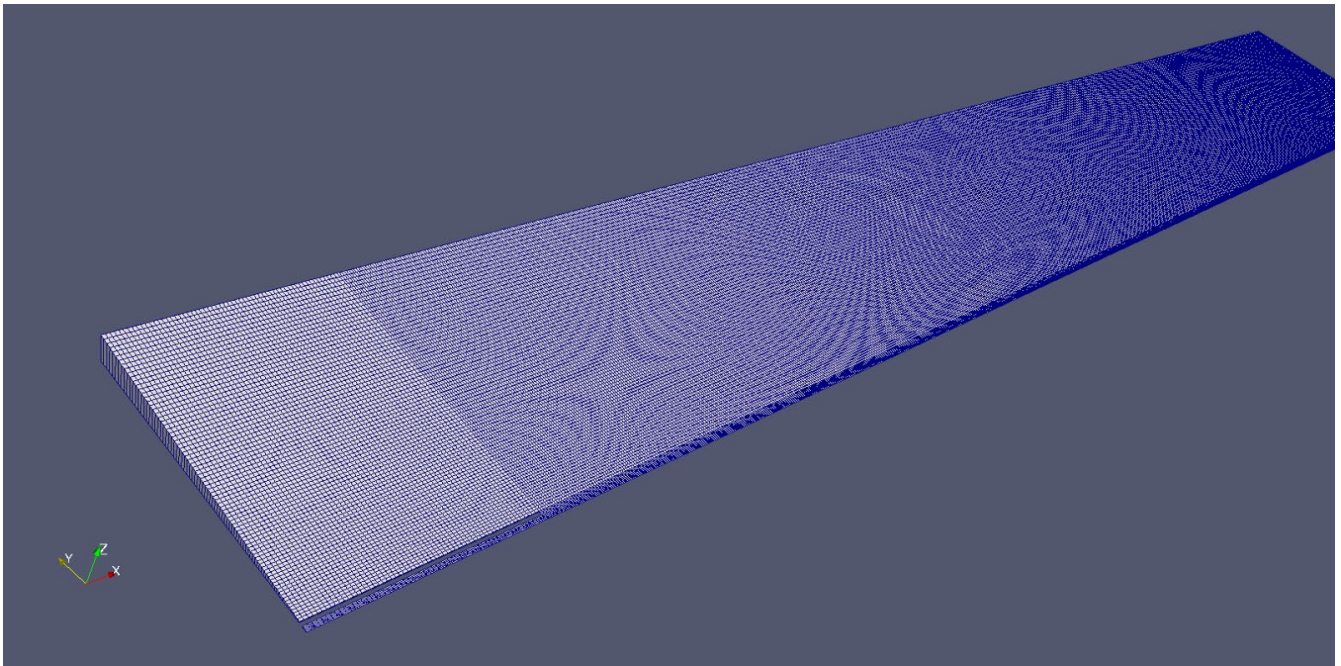


Figure 31. Schematic of Mesh B.

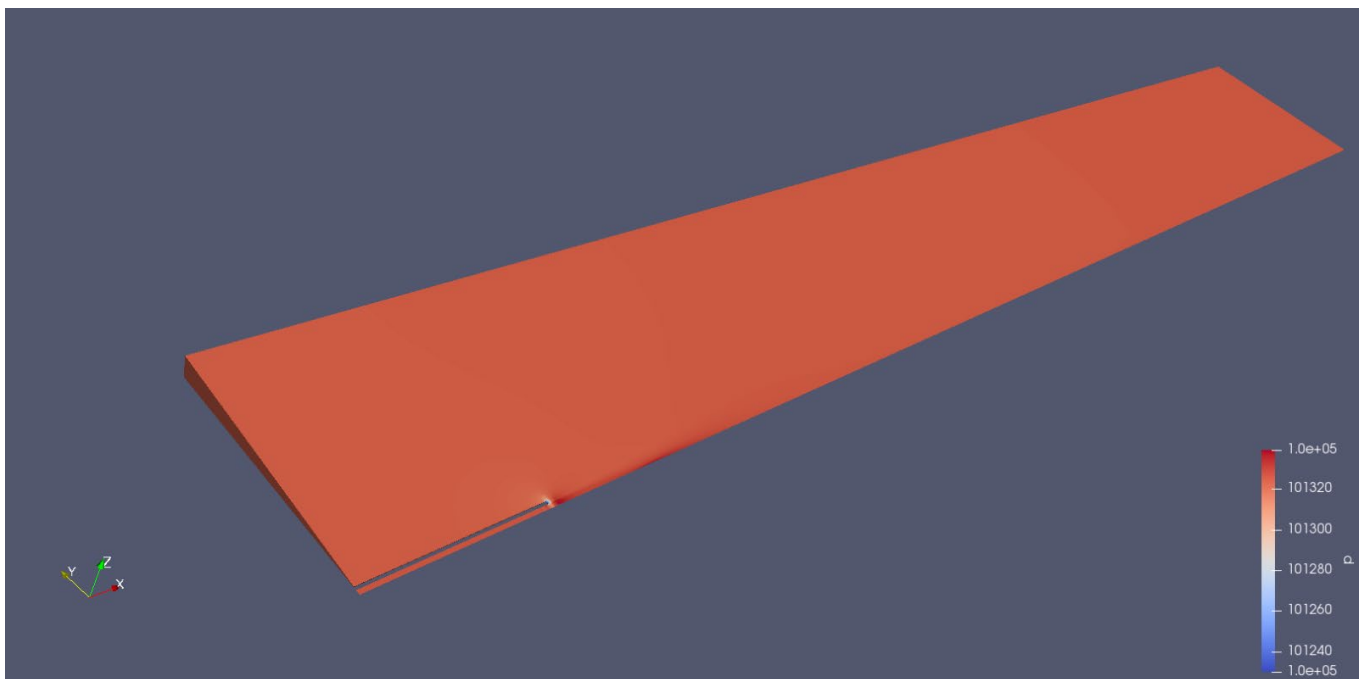


Figure 32. Pressure (Mesh B).

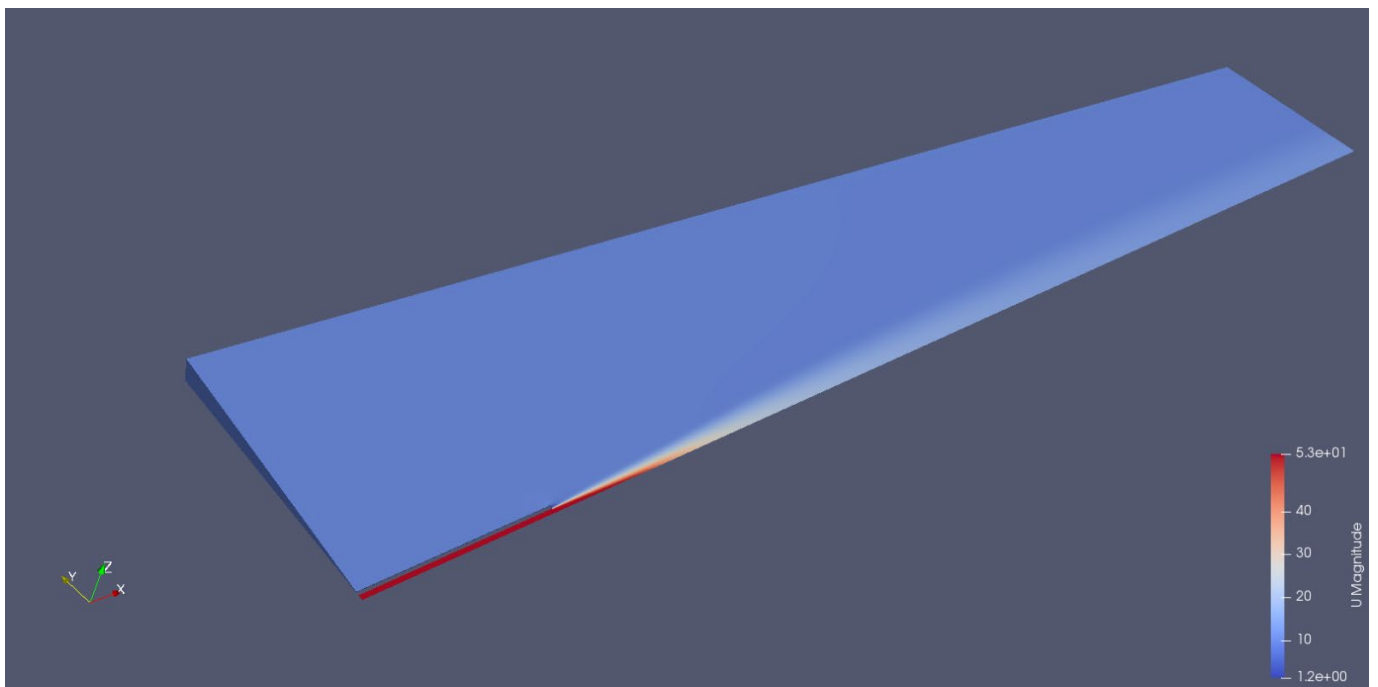


Figure 33. Velocity (Mesh B).



Figure 34. Velocity (Mesh B).

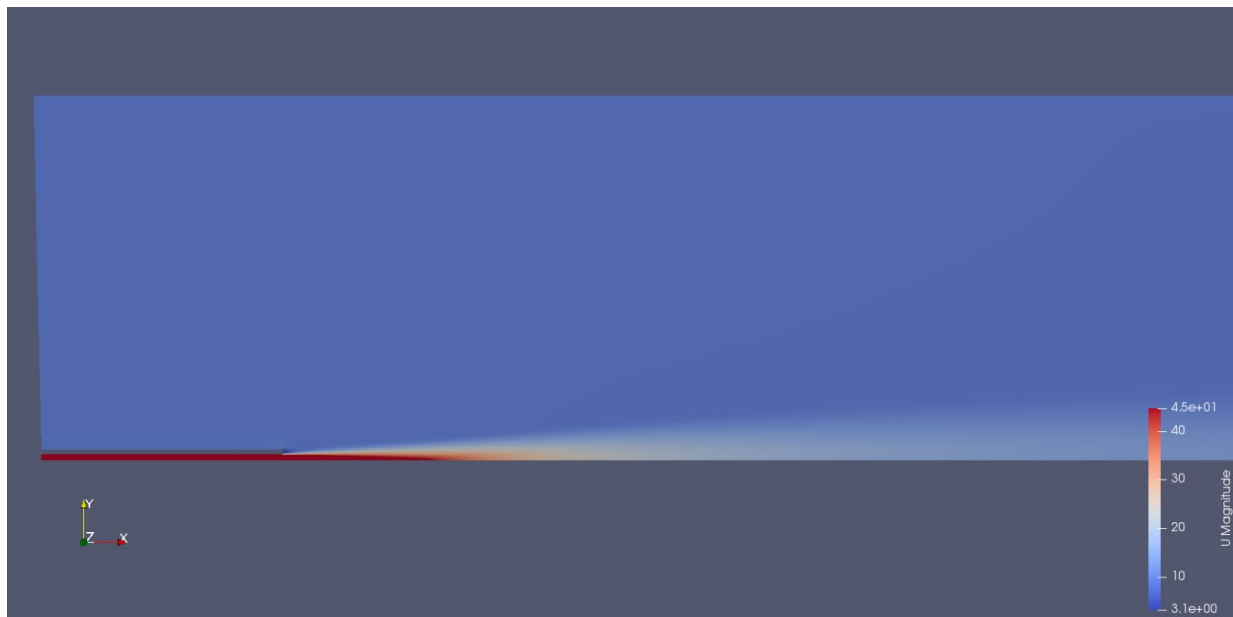


Figure 35. Velocity (Mesh B).

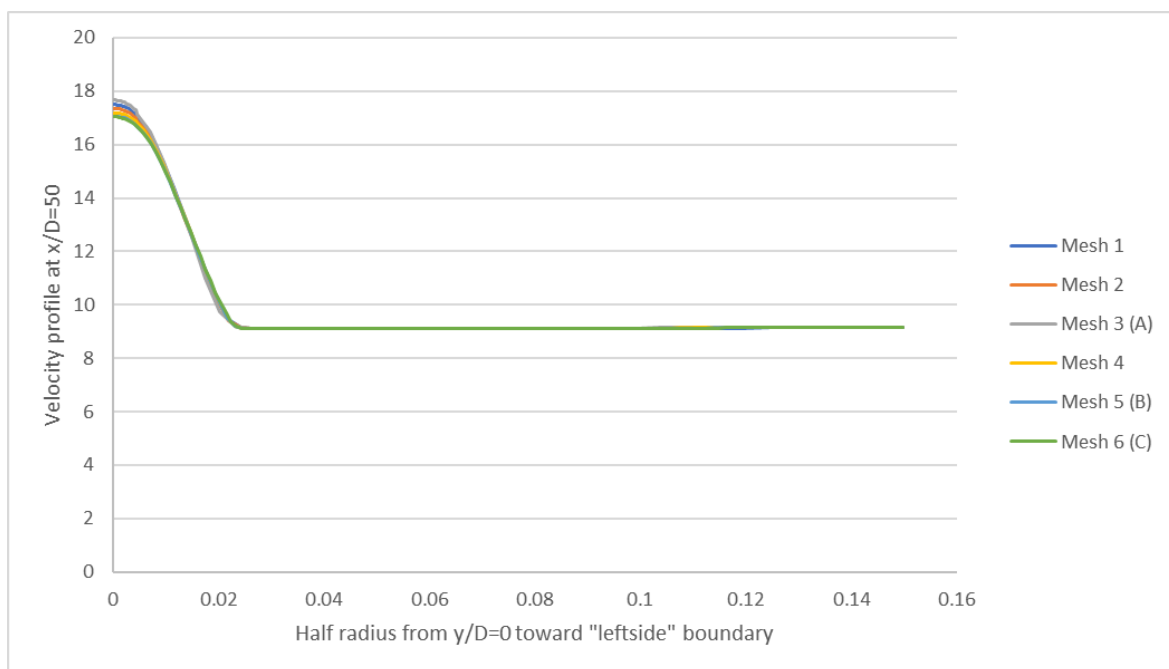


Figure 36. Mesh independency comparison for a half radius of the velocity profile at $x/D = 50$.

Author Contributions: Conceptualization, A.A. and S.K.; Methodology, A.A. and S.K.; Software, A.A.; Validation, A.A.; Formal analysis, A.A.; Investigation, A.A. and S.K.; Resources, A.A. and S.K.; Data curation, A.A.; Writing—Original draft preparation, A.A.; Writing—Review and editing, S.K.; Visualization, A.A.; Supervision, S.K.; Project administration, S.K. All authors have read and agreed to the published version of the manuscript.

Funding: This research received no external funding.

Institutional Review Board Statement: Not applicable.

Informed Consent Statement: Not applicable.

Data Availability Statement: All the codes and results of the study have been placed on Google Drive, making it possible for other researchers to use and build upon these findings: <https://>

drive.google.com/drive/folders/16QSF0qvg4GE5PnspN4Y8KzaLbihUFYa?usp=sharing (accessed on 10 March 2023).

Conflicts of Interest: The authors declare no conflict of interest.

References

1. Kannan, B. Computation of an axisymmetric jet using OpenFOAM. *Procedia Eng.* **2015**, *127*, 1292–1299.
2. Imine, B.; Imine, O.; Abidat, M.; Liazid, A. Study of non-reactive isothermal turbulent asymmetric jet with variable density. *Comput. Mech.* **2006**, *38*, 151–162. [[CrossRef](#)]
3. Schefer, R.; Dibble, R. Mixture fraction field in a turbulent nonreacting Propane jet. *AIAA J.* **2001**, *39*, 64–72. [[CrossRef](#)]
4. Wagnanski, I.; Fiedler, H. Some measurements in the self-preserving jet. *J. Fluid Mech.* **1969**, *38*, 577–612. [[CrossRef](#)]
5. Becker, H.A.; Hottel, H.C.; Williams, G.C. The nozzle-fluid concentration field of the round, turbulent, free jet. *J. Fluid Mech.* **1967**, *30*, 285–303. [[CrossRef](#)]
6. Shaughnessy, E.; Morton, J. Laser light-scattering measurements of particle concentration in a turbulent jet. *J. Fluid Mech.* **1977**, *80*, 129–148. [[CrossRef](#)]
7. Dowling, D.R.; Lang, D.B.; Dimotakis, P.E. An improved Laser-Rayleigh Scattering photodetection system. *Exp. Fluids* **1989**, *7*, 435–440. [[CrossRef](#)]
8. Dowling, D.R.; Dimotakis, P.E. Similarity of the concentration field of gas-phase turbulent jets. *J. Fluid Mech.* **1990**, *218*, 109–141. [[CrossRef](#)]
9. Fulachier, L.; Anselmet, F.; Amielh, M. *Turbulent Jets with Variable Density, PRC Combustion in the Rocket Motors Cryotechnic*; CNRS/CNES/SEF: Paris, France, 1990.
10. Gazzah, M.H.; Sassi, M.; Sarh, B.; Gökalp, I. Simulation numérique des jets turbulents subsoniques à masse volumique variable par le modèle $k-\epsilon$. *Int. J. Therm. Sci.* **2002**, *41*, 51–62. [[CrossRef](#)]
11. Gouldin, F.C.; Schefer, R.W.; Johnson, S.C.; Kollmann, W. Nonreacting turbulent mixing flows. *Prog. Energy Combust. Sci.* **1986**, *12*, 257–303. [[CrossRef](#)]
12. Panchapakesan, N.; Lumley, J. Turbulence measurements in axisymmetric jets of air and helium. Part 1. Air jet. *J. Fluid Mech.* **1993**, *246*, 197–223. [[CrossRef](#)]
13. Panchapakesan, N.; Lumley, J. Turbulence measurements in axisymmetric jets of air and helium. Part 2. Helium jet. *J. Fluid Mech.* **1993**, *246*, 225–247. [[CrossRef](#)]
14. Pietri, L.; Amielh, M.; Anselmet, F. Simultaneous measurements of temperature and velocity fluctuations in a slightly heated jet combining a cold wire and Laser Doppler Anemometry. *Int. J. Heat Fluid Flow* **2000**, *21*, 22–36. [[CrossRef](#)]
15. Purwanto, A. Modélisation d'écoulements Turbulents-Basse Vitesse à Forte Variation de Masse Volumique: Application aux Schémas de Fermeture Kappa-Epsilon. Ph.D. Thesis, INPT, Toulouse, France, 1994.
16. So, R.M.C.; Zhu, J.Y.; Ötügen, M.V.; Hwang, B.C. Some measurements in a binary gas jet. *Exp. Fluids* **1990**, *9*, 273–284. [[CrossRef](#)]
17. Thring, M.; Newby, M. Combustion length of enclosed turbulent flames. In *Fourth Symposium (International) on Combustion*; The Williams & Wilkins Co., Ltd.: London, UK, 1953.
18. Stårner, S.H.; Bilger, R.W.; Dibble, R.W.; Barlow, R.S. Piloted Diffusion Flames of Diluted Methane Near Extinction: Mean Structure from Raman/Rayleigh Fluorescence Measurements. *Combust. Sci. Technol.* **1990**, *70*, 111–133. [[CrossRef](#)]
19. Meier, W.; Vyrodov, A.O.; Bergmann, V.; Stricker, W. Simultaneous Raman/LIF measurements of major species and NO in turbulent H₂/air diffusion flames. *Appl. Phys. B* **1996**, *63*, 79–90. [[CrossRef](#)]
20. Mhiri, H.; Habli, S.; El Golli, S.; Le Palec, G.; Bournot, P. Etude numérique des conditions d'émission sur un écoulement de type jet plan turbulent isotherme ou chauffé. *Int. J. Therm. Sci.* **1999**, *38*, 904–915. [[CrossRef](#)]
21. Gonçalves, V.; Magalhães, G.; Vedovotto, J. URANS Simulation of Turbulent Non-premixed and Non-reacting Propane Jet Flow. In Proceedings of the 12th Spring School on Transition and Turbulence, EPTT 2020, Blumenau, Brazil, 21–25 September 2020. [[CrossRef](#)]
22. Ouzani, R.; Si-Ameur, M.; Khelladi, S.; Danlos, A. Mixing in turbulent compressible heated coaxial jets: A numerical study. *Int. J. Hydrog. Energy* **2020**, *45*, 16816–16837. [[CrossRef](#)]
23. Fluent, A. *ANSYS Fluent Theory Guide 15.0*; ANSYS: Canonsburg, PA, USA, 2013.
24. Versteeg, H.K.; Malalasekera, W. *An Introduction to Computational Fluid Dynamics: The Finite Volume Method*; Pearson Education: London, UK, 2007.
25. Marzouk, O.A.; Huckaby, E.D. Simulation of a Swirling Gas-Particle Flow Using Different $k-\epsilon$ Models and Particle-Parcel Relationships. *Eng. Lett.* **2010**, *18*, 7.
26. Nebenführ, B. OpenFOAM: A Tool for Predicting Automotive Relevant Flow Fields. Master's Thesis, Chalmers University of Technology, Gothenburg, Sweden, 2010.

Disclaimer/Publisher's Note: The statements, opinions and data contained in all publications are solely those of the individual author(s) and contributor(s) and not of MDPI and/or the editor(s). MDPI and/or the editor(s) disclaim responsibility for any injury to people or property resulting from any ideas, methods, instructions or products referred to in the content.